RESEARCH ARTICLE SUMMARY

CANCER IMMUNOLOGY

# Deterministic reprogramming of neutrophils within tumors

**Melissa S. F. Ng†*, Immanuel Kwok†, Leonard Tan†, Changming Shi†, Daniela Cerezo-Wallis, Yingrou Tan, Keith Leong, Gabriel F. Calvo, Katharine Yang, Yuning Zhang, Jingsi Jin, Ka Hang Liong, Dandan Wu, Rui He, Dehua Liu, Ye Chean Teh, Camille Bleriot, Nicoletta Caronni, Zhaoyuan Liu, Kaibo Duan, Vipin Narang, Iván Ballesteros, Federica Moalli, Mengwei Li, Jinmiao Chen, Yao Liu, Lianxin Liu, Jingjing Qi, Yingbin Liu, Lingxi Jiang, Baiyong Shen, Hui Cheng, Tao Cheng, Veronique Angeli, Ankur Sharma, Yuin-han Loh, Hong Liang Tey, Shu Zhen Chong, Matteo Iannacone, Renato Ostuni, Andrés Hidalgo, Florent Ginhoux, Lai Guan Ng***

**INTRODUCTION:** Neutrophils are the first responders to infection and injury and are rapidly recruited to affected tissues in large numbers to enact their protective function. As such, neutrophils were historically perceived as a homogeneous and transient population. Recently, however, a diverse array of neutrophil states has been reported in cancer, varying in their maturation, surface marker expression, and transcript profiles. The relationship between these neutrophil states and their organization into a unified protumoral response have yet to be elucidated, limiting the therapeutic targeting of neutrophils in cancer.

**RATIONALE:** To identify the mechanisms by which disparate neutrophil states are coordinated into a concerted protumoral response, we used single-cell RNA sequencing and ATACseq (assay for transposable chromatin sequencing) on neutrophils from various organs and tumors in a murine orthotopic model of pancreatic cancer. Tumor neutrophil states identified from these analyses were validated by multiparametric flow cytometry, and spatial mapping at the RNA and protein levels were performed to reveal their localization within the pancreatic tumors. In vitro and in vivo approaches were then used to examine how the tumor environment shapes neutrophil phenotype, lifespan, and protumoral functions.

**RESULTS:** We identified three distinct neutrophil states within the tumor microenvironment, T1, T2, and T3, which were epigenetically and transcriptionally distinct from neutrophils in the bone marrow, spleen, and blood. By assessing nuclear morphology and maturation status, we determined that immature and mature neutrophils infiltrating the tumor differentiated into transitional T1 and T2 populations, respectively. T1 and T2 neutrophils underwent further reprogramming to converge into the T3 neutrophil state, which was terminally differentiated and expressed the surface marker dcTRAIL-R1. dcTRAIL-R1 up-regulation in tumor-naïve neutrophils could be induced by exposure to tumor-conditioned medium in vitro or entry into the tumor in vivo, and was accompanied by the expression of T3-specific genes. More importantly, this phenomenon was independent of their initial maturation phenotype. These findings thus underscore the capability of neutrophils to adopt a new functional phenotype, overlaying it onto their existing differentiation stage. The T3 phenotype was strongly correlated with a prolonged lifespan, with dcTRAIL-R1$^+$ neutrophils persisting for more than 5 days within the tumor. Furthermore, T3 neutrophils were mainly localized to a unique hypoxic-glycolytic niche within the tumor, where they optimally exerted their pro-angiogenic function. This indicated that neutrophil reprogramming plays a critical role in enabling their survival under hypoxia, oxidative stress, and metabolic perturbations within the tumor microenvironment. Specifically, T3 neutrophils expressed high levels of vascular endothelial growth factor alpha (VEGFα) and substantially enhanced blood vessel formation within the tumor core, and only coinjection of T3 neutrophils with tumor cells accelerated tumor growth. Therefore, the ablation of either T3 neutrophils or VEGFα inhibits this growth enhancement. Finally, all three tumor neutrophil states were observed across mouse models and in multiple human cancers, with the T3 signature predicting poorer patient outcomes in two independent human pancreatic cancer cohorts and other solid tumor types.

**CONCLUSION:** By examining neutrophils in the context of their ontogeny, we uncovered their intrinsic flexibility in adapting to environmental signals regardless of their initial maturation stage. This implies that neutrophils infiltrating a tissue niche follow a common path, merging their different functional states into a single terminal phenotype as guided by the tissue. Within the tumor, this deterministic program likely ensures a continual supply of pro-angiogenic T3 neutrophils that fuel tumor growth. Our findings thus demonstrate how short-lived effector cells such as neutrophils effectively tailor their functions to accommodate tissue requirements, highlighting the untapped possibilities of targeting the local neutrophil response as immunotherapy. ■

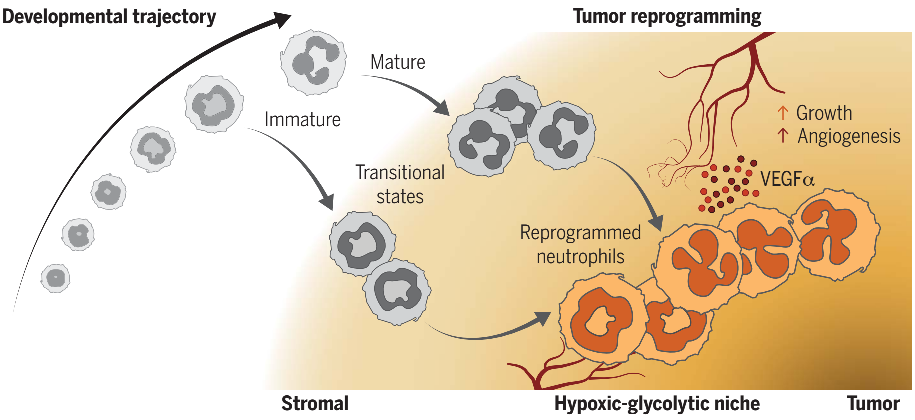

**Tumor-infiltrating neutrophils undergo convergent reprogramming into pro-angiogenic neutrophils that support tumor growth.** In cancer, both immature and mature neutrophils infiltrate the tumor. After entering the tumor microenvironment, these neutrophils undergo differentiation, leading to the formation of transitional populations. Through reprogramming, these populations ultimately converge into a terminal neutrophil state. Reprogrammed neutrophils strongly express VEGFα and localize to a unique hypoxic-glycolytic niche near the tumor core. This places them in an optimal position to exert their pro-angiogenic function within hypoxic and nutrient-poor tumor regions, thereby promoting tumor growth. The emergence of tumor reprogramming reflects the adaptability of neutrophils to environmental cues, allowing them to consolidate their protumoral responses.

---

The list of author affiliations is available in the full article online.
*Corresponding author. Email: nglaiguan@renji.com (L.G.N.); melissa_ng@immunol.a-star.edu.sg (M.S.F.N.)
†These authors contributed equally to this work.

Cite this article as M. S. F. Ng *et al.*, *Science* **383**, eadf6493 (2024). DOI: 10.1126/science.adf6493

READ THE FULL ARTICLE AT
https://doi.org/10.1126/science.adf6493

RESEARCH ARTICLE

CANCER IMMUNOLOGY

# Deterministic reprogramming of neutrophils within tumors

**Melissa S. F. Ng[1]*†, Immanuel Kwok[1]†, Leonard Tan[1]†, Changming Shi[2]†, Daniela Cerezo-Wallis[3,4], Yingrou Tan[1,5], Keith Leong[1], Gabriel F. Calvo[6], Katharine Yang[1], Yuning Zhang[7,8], Jingsi Jin[2], Ka Hang Liong[1], Dandan Wu[9], Rui He[2], Dehua Liu[1], Ye Chean Teh[1], Camille Bleriot[10,11], Nicoletta Caronni[12], Zhaoyuan Liu[9], Kaibo Duan[1], Vipin Narang[1], Iván Ballesteros[3], Federica Moalli[13,14], Mengwei Li[1], Jinmiao Chen[1], Yao Liu[15], Lianxin Liu[15], Jingjing Qi[16,17], Yingbin Liu[16,17], Lingxi Jiang[18,19,20], Baiyong Shen[18,19,20], Hui Cheng[21], Tao Cheng[21], Veronique Angeli[7,8], Ankur Sharma[22,23,24], Yuin-han Loh[25], Hong Liang Tey[5,26,27], Shu Zhen Chong[1,28], Matteo Iannacone[13,14,29], Renato Ostuni[12,29], Andrés Hidalgo[3,4], Florent Ginhoux[1,9,10,30], Lai Guan Ng[2,1,28]***

**Neutrophils are increasingly recognized as key players in the tumor immune response and are associated with poor clinical outcomes. Despite recent advances characterizing the diversity of neutrophil states in cancer, common trajectories and mechanisms governing the ontogeny and relationship between these neutrophil states remain undefined. Here, we demonstrate that immature and mature neutrophils that enter tumors undergo irreversible epigenetic, transcriptional, and proteomic modifications to converge into a distinct, terminally differentiated dcTRAIL-R1$^+$ state. Reprogrammed dcTRAIL-R1$^+$ neutrophils predominantly localize to a glycolytic and hypoxic niche at the tumor core and exert pro-angiogenic function that favors tumor growth. We found similar trajectories in neutrophils across multiple tumor types and in humans, suggesting that targeting this program may provide a means of enhancing certain cancer immunotherapies.**

Neutrophils play a substantial role in the immune response to infection and injury. As one of the first cells to enter a damaged site from the circulation, the rapid recruitment of large numbers of neutrophils into the tissue is key for their protective function (*1*). This process is co-opted in pathological settings such as cancer, in which persistent neutrophil infiltration into the tumor has been consistently associated with poorer patient outcomes (*2*). Many studies have associated protumoral functions to neutrophils, which in this context have been referred to as granulocytic myeloid-derived suppressor cells (*3*). This uniform view has since been disrupted by the identification of a wide spectrum of neutrophil states in cancer, with differences in density (*4*, *5*), surface markers (*6*–*10*), and transcript expression (*11*–*13*).

Neutrophil heterogeneity also exists in the bone marrow (BM) in the form of various maturation stages. Numerous studies have shown that granulocytic progenitor cells differentiate sequentially into precursor, immature, and finally mature neutrophils, and each subset of cells has distinct functional capabilities (*14*–*19*). Tumor-induced chronic inflammation triggers the premature egress of these precursors into the circulation and subsequently into the tumor (*4*, *14*, *17*, *19*, *20*), and extramedullary sites such as the spleen (*13*, *14*), have been proposed to be priming sites of protumoral neutrophils (*12*, *21*, *22*). Collectively, this spectrum of neutrophil states, encompassing phenotypic and maturation differences, is proposed to make up the functional diversity of neutrophils in cancer (*4*–*15*).

Here, we used multi-omics approaches in pancreatic tumors at single-cell transcriptional and spatial resolution to examine neutrophil functional diversity in the context of their ontogenetic order, origin, and influence from tissue signals. We unexpectedly found that although various populations of neutrophils entered the tumor, it was only inside the tumor that neutrophils entered a convergent trajectory that directed them toward a specific protumoral state. Our findings challenge current models and suggest the potential of targeting neutrophils for cancer immunotherapy.

## Intratumoral neutrophils converge into a distinct transcriptional state

To investigate neutrophil heterogeneity in cancer, we used an orthotopic mouse model of pancreatic ductal adenocarcinoma (PDAC). Using a pancreatic cancer cell line previously established from a tumor in the $Pdx1^{Cre}$; $Kras^{G12D/+}$; $Trp53^{R172H/+}$ (KPC) genetically modified mouse model (*23*), cultured cells were orthotopically transplanted into the pancreas, which grew in situ to form a tumor characterized by copious neutrophil infiltration (*14*). Single-cell RNA sequencing (scRNAseq) was performed on total $CD11b^+CD115^-Ly6G^+$ cells from the BM, spleen, blood, and pancreatic tumors to characterize neutrophil heterogeneity in the context of their ontogenetic order and origin ($n = 2$; Fig. 1A and fig. S1, A and B). Uniform manifold approximation and projection (UMAP) analysis revealed that neutrophils from the BM, spleen, and blood clustered according to their developmental states, from pre-neutrophils (preNeus) to immature neutrophils (IMM 1 and 2) and mature neutrophils (MAT 1 to 5) (Fig. 1B and fig. S1C). Integration with a previous dataset containing healthy mouse neutrophils from matching tissues (*19*) showed that despite

---

[1]Singapore Immunology Network (SIgN), Agency for Science, Technology and Research (A*STAR), Singapore. [2]Shanghai Immune Therapy Institute, Renji Hospital, Shanghai Jiao Tong University School of Medicine, Shanghai, China. [3]Area of Cell & Developmental Biology, Centro Nacional de Investigaciones Cardiovasculares Carlos III, Madrid, Spain. [4]Vascular Biology and Therapeutics Program and Department of Immunobiology, Yale University School of Medicine, New Haven, CT, USA. [5]National Skin Centre, National Healthcare Group, Singapore. [6]Department of Mathematics & MOLAB-Mathematical Oncology Laboratory, University of Castilla-La Mancha, Ciudad Real, Spain. [7]Immunology Translational Research Program, Department of Microbiology and Immunology, Yong Loo Lin School of Medicine, National University of Singapore, Singapore. [8]Immunology Program, Life Science Institute, National University of Singapore, Singapore. [9]Shanghai Institute of Immunology, Shanghai Jiao Tong University School of Medicine, Shanghai, China. [10]INSERM U1015, Institut Gustave Roussy, Villejuif, France. [11]CNRS UMR8253, Institut Necker des Enfants Malades, Paris, France. [12]Genomics of the Innate Immune System Unit, San Raffaele-Telethon Institute for Gene Therapy (SR-Tiget), IRCCS San Raffaele Scientific Institute, Milan, Italy. [13]Division of Immunology, Transplantation, and Infectious Diseases, IRCCS San Raffaele Scientific Institute, Milan, Italy. [14]Experimental Imaging Centre, IRCCS San Raffaele Scientific Institute, Milan, Italy. [15]Department of Hepatobiliary Surgery, The First Affiliated Hospital of USTC, Division of Life Sciences and Medicine, University of Science and Technology of China, Anhui, China. [16]Department of Biliary and Pancreatic Surgery, Renji Hospital, Shanghai Jiao Tong University School of Medicine, Shanghai, China. [17]Shanghai Institute of Cancer Biology, Renji Hospital, Shanghai Jiao Tong University School of Medicine, Shanghai, China. [18]Department of General Surgery, Pancreatic Disease Center, Ruijin Hospital, Shanghai Jiao Tong University School of Medicine, Shanghai, China. [19]Research Institute of Pancreatic Diseases, Shanghai Key Laboratory of Translational Research for Pancreatic Neoplasms, Shanghai Jiao Tong University School of Medicine, Shanghai, China. [20]State Key Laboratory of Oncogenes and Related Genes, Institute of Translational Medicine, Shanghai Jiao Tong University, Shanghai, China. [21]State Key Laboratory of Experimental Hematology, National Clinical Research Center for Blood Diseases, Haihe Laboratory of Cell Ecosystem, Institute of Hematology & Blood Diseases Hospital, Chinese Academy of Medical Sciences & Peking Union Medical College, Tianjin, China. [22]Harry Perkins Institute of Medical Research, QEII Medical Centre, Nedlands, Western Australia, Australia. [23]Curtin Medical School, Curtin University, Bentley, Western Australia, Australia. [24]Curtin Health Innovation Research Institute, Curtin University, Bentley, Western Australia, Australia. [25]Institute of Molecular and Cell Biology (IMCB), A*STAR (Agency for Science, Technology and Research), Singapore. [26]Lee Kong Chian School of Medicine, Nanyang Technological University, Singapore. [27]Yong Loo Lin School of Medicine, National University of Singapore, Singapore. [28]Department of Microbiology and Immunology, National University of Singapore, Singapore. [29]Vita-Salute San Raffaele University, Milan, Italy. [30]Translational Immunology Institute, SingHealth Duke-NUS Academic Medical Centre, Singapore.
***Corresponding author. Email: nglaiguan@renji.com (L.G.N.); melissa_ng@immunol.a-star.edu.sg (M.S.F.N.)**
†These authors contributed equally to this work.

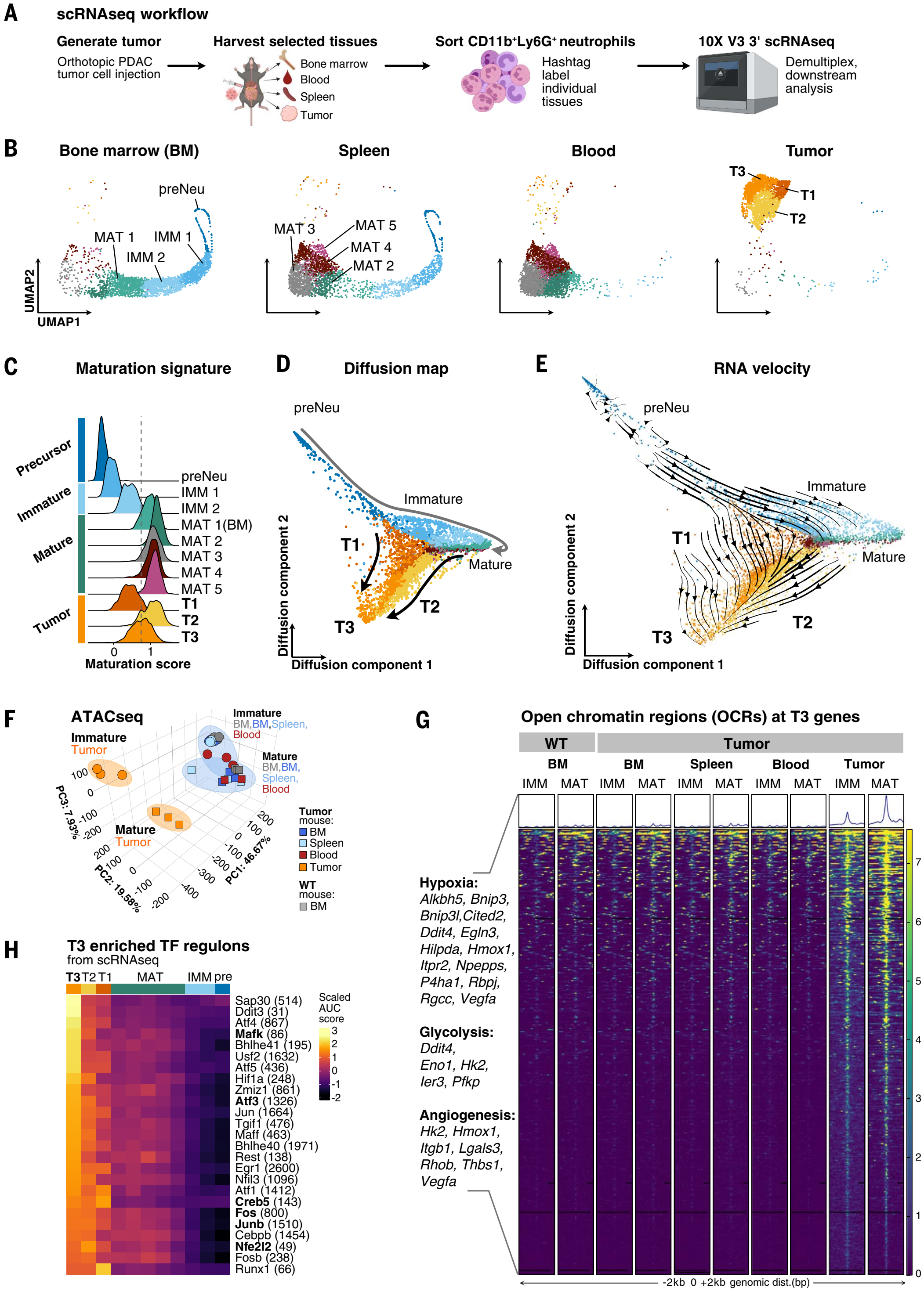

**Fig. 1. Neutrophils infiltrate pancreatic tumors and undergo further differentiation and converge upon a transcriptionally distinct T3 neutrophil state.** (**A**) Schematic showing scRNAseq workflow. CD11b$^+$Ly6G$^+$ neutrophils were sorted from the BM, spleen, blood, and pancreatic tumor of tumor-bearing mice 6 weeks after orthotopic injection (*n* = 2 biological replicates). Each sample was individually tagged with cell-hashing antibodies before being pooled for analysis with 10X V3 3′ scRNAseq (see also fig. S1A and the materials and methods). (**B**) UMAP projection of total neutrophils in the BM, spleen, blood, and tumor show strong enrichment of three clusters (T1, T2, and T3) in the tumor. Louvain clustering was performed, and colors correspond to the clusters identified. (**C**) The neutrophil maturation score can be used to identify Louvain clusters along their differentiation trajectory. Histograms show the module score of the maturation gene signature for each cluster identified in (B), with scores closest to 1 being the most mature. Dotted line in gray defines the cutoff for mature neutrophils and is set at the lower bound of the Mature 2 cluster. (**D**) Low dimensional embedding of all neutrophils using a diffusion map approach reveals a branch point between mature and tumor neutrophils. Scatterplot shows diffusion components 1 and 2. Light gray arrows are used to indicate the trajectory from precursor, immature, and mature neutrophil states. Black arrows denote the branching into T3 neutrophils from T1 and T2 states. (**E**) RNA velocity suggests the convergent differentiation of T1 and T2 into T3 neutrophils. RNA velocity vectors were projected on the diffusion map embedding with velocity vectors terminating in the tumor and mature neutrophils. (**F**) Principal component analysis of ATACseq indicated that changes in chromatin accessibility established in tumor neutrophils clustered them away from other neutrophil subsets. ATACseq was performed for immature (circles) and mature (squares) neutrophils sorted from the BM (gray and dark blue, *n* = 3 each), spleen (light blue, *n* = 3 each), blood (red, *n* = 3 mature, *n* = 2 immature), and tumor (orange, *n* = 3 each) in wild-type (WT) or tumor-bearing (tumor) mice. Numbers denote the number of biological replicates used. (**G**) OCRs matched to differentially expressed T3 genes have increased accessibility only in immature and mature tumor neutrophils. Heatmap shows intensity of fragment mapping across indicated neutrophil subsets; histograms indicate average mapping intensity. T3 genes linked to hypoxia, glycolysis, and angiogenesis are annotated (see also table S2). (**H**) Heatmap showing scaled AUC scores of the top 25 transcription factor regulons enriched in T3 neutrophils computed by PySCENIC (see also table S2). Numbers in brackets denote the number of genes assigned to the transcription factor regulon. Transcription factors that also had increased motif enrichment in tumor-associated immature and mature bulk neutrophil populations are shown in bold.

potential perturbations from the tumor, no new developmental clusters or trajectories emerged in neutrophils from tissues of the tumor-bearing mice (fig. S1, D and E). This suggests a robust adhesion of neutrophils to a single developmental trajectory within the tissues where they develop and circulate. By contrast, neutrophils acquired specific transcriptional profiles in the tumor (Fig. 1B and fig. S1C) and formed three distinct clusters (T1, T2, and T3) separate from the other compartments.

Because immature and mature neutrophils can infiltrate tumoral tissue ([14], [15]), we investigated the relationship between the maturation and functional states of the T1 to T3 neutrophil populations using a neutrophil maturation gene signature (table S1) curated by Xie *et al.* ([19]); each cluster in our dataset was graded by a maturation score. T1 neutrophils had a maturation score comparable to immature neutrophils (i.e., the IMM 2 cluster), whereas T2 neutrophils had a maturation score similar to mature neutrophils (i.e., the MAT 1 to 5 clusters) (Fig. 1C). Next, we sought to uncover more potential links between neutrophil clusters in the tumor and the other tissue compartments by using a diffusion map approach that orders cells on the basis of transitional probabilities and better preserves differentiation trajectories ([24], [25]). We found that tumor neutrophils deviated from the steady-state neutrophil developmental trajectory (Fig. 1D). Specifically, T1 and T2 neutrophils progressed along the tumor-specific branch and converged at the T3 state, suggesting that T1 and T2 may both give rise to the T3 population, which is predicted to be the most terminally differentiated subset. RNA velocity ([26]) indicated a pseudotime progression from immature neutrophils to T1 and mature neutrophils to T2, suggesting that T1 and T2 neutrophils are transitory states from immature and mature neutrophils that have migrated into the tumor (Fig. 1E). By contrast, T3 neutrophils exhibited a maturation score that was in between that of the T1 and T2 neutrophils (Fig. 1C), representing a potential admixture of T1 and T2 cells. Accordingly, we observed that velocity vectors originating from both T1 and T2 populations terminated in the T3 cluster (Fig. 1E). These findings thus corroborate earlier studies demonstrating that both mature and immature neutrophils infiltrate tumor tissue ([4]) and become T1 and T2 neutrophils, respectively. Further, our data predict that these stages are transitional, because both T1 and T2 neutrophils remained amendable for further differentiation into T3 neutrophils.

### Epigenetic reprogramming of tumor-infiltrating neutrophils

To confirm that T3 neutrophils can be reprogrammed from both immature (T1) and mature (T2) tumor neutrophils, we performed ATACseq (assay for transposase-accessible chromatin followed by sequencing) on sorted CD101$^-$ (immature) and CD101$^+$ (mature) neutrophils ([14]) from various tissue compartments of control and tumor-bearing mice. Principal component analysis revealed that both immature and mature tumor neutrophils clustered separately from corresponding subsets of neutrophils from other tissues (Fig. 1F), indicating that signals from the tumor microenviroment imprint specific chromatin accessibility changes within infiltrating neutrophils. We then identified all open chromatin regions (OCRs) that were differentially accessible in immature and mature tumor neutrophils relative to the nontumor neutrophil subsets (table S2). Increased chromatin accessibility for genes up-regulated in T3 neutrophils (T3 genes) in both immature and mature tumor neutrophils (Fig. 1G) included genes involved with hypoxia, glycolysis, and angiogenesis, such as *Vegfa* and *Hk2* (fig. S2A). These changes in chromatin were undetectable in neutrophils from other tissues, which still shared similar accessibility for canonical neutrophil genes such as *Cebpa* and *Gfi1* (fig. S2B).

To elucidate putative upstream regulators of the T3 program, we used pySCENIC ([27]) to identify transcription factor regulons predicted in T3 neutrophils that had minimal presence in the other neutrophil subsets (Fig. 1H). This was then correlated to motifs found in the bulk ATACseq analysis (fig. S2C), which revealed T3-specific transcription factors with enriched motifs in immature and mature tumor neutrophil differentially accessible OCRs (fig. S2, D and E). Among the T3-specific transcription factors, *Mafk*, *Nfe2l2*, and *Atf3* were implicated in regulating metabolic and oxidative stress typical of the tumor microenvironment (fig. S2, D and E). Correlation of the underlying chromatin accessibility with transcription factors predicted to govern the T3 state suggested that these epigenetic changes initiated within T1 and T2 neutrophils are reinforced by transcription factor activity as they transition toward a T3 state. These findings suggest that tumor-infiltrating neutrophils can be reprogrammed by the tumor microenvironment regardless of their stage of maturity by converging transcriptional and chromatin trajectories toward a distinct T3 state.

### CD101 and dcTRAIL-R1 discriminate tumor neutrophil states

Having shown that immature T1 and mature T2 neutrophils in the tumor undergo transcriptional and epigenetic reprogramming toward the T3 neutrophils, we next assessed whether we could distinguish these subsets by protein expression. This was particularly important because increases in RNA expression in neutrophils typically precedes protein expression, especially for genes tightly regulated in neutrophil development, such as those for granule proteins ([14]). T1, T2, and T3 neutrophils had differential expression of surface marker genes, suggesting that a combination of surface marker protein staining could be used to identify them (fig. S3A). Using a multiparametric flow cytometry approach, live CD45$^+$ cells from the PDAC tumor were screened for 249 cell surface markers. Then, all captured cells were clustered with InfinityFlow ([28], [29]), and the coexpression patterns of all tested markers were evaluated (fig. S3B), which revealed two distinct neutrophil clusters (Fig. 2A). High levels of immuno-modulatory or suppressive markers such as dcTRAIL-R1, PD-L1 (CD274) ([6]), CD14 ([13]), CD371 ([30]), VISTA ([31]), and CD39 ([32]), distinguished Cluster 2 neutrophils from those of Cluster 1 (Fig. 2B). These markers correlated with surface marker genes enriched in T3 neutrophils (fig. S3C), suggesting that they may serve to identify the T3 state. Indeed, we found that dcTRAIL-R1 was expressed mainly by a population of tumor neutrophils (Fig. 2C) while having minimal expression in tumor-infiltrating monocytes and macrophages and in neutrophils in the BM, spleen, and blood (Fig. 2C and fig. S3D). By contrast, staining for other markers such as VISTA and CD14 showed expression across multiple neutrophil subsets and was less restricted to tumor neutrophils (Fig. 2D and fig. S3D). dcTRAIL-R1 expression in tumor-infiltrating neutrophils was also conserved across several other tumor types, including orthotopic breast cancer [median: 20.4%; interquartile range (IQR): 18.0 to 23.1%] and orthotopic lung cancer (median: 12.1%; IQR: 4.54 to 19.5%) mouse models (fig. S3E). Across all experimental tumor models examined, dcTRAIL-R1 expression was similarly limited to a subset of tumor neutrophils, suggesting a possible candidate marker for T3 neutrophils.

Consistent with its protein expression pattern, gene expression and RNA velocity (indicative of active gene transcription) for the gene encoding dcTRAIL-R1 (*Tnfrsf23*) were highest in the T3 neutrophil cluster (fig. S4A). Therefore, we attributed the T3 population to the dcTRAIL-R1$^+$ cluster (cluster 2), whereas the T1 and T2 populations were likely contained within the dcTRAIL-R1$^-$ cluster (cluster 1) identified in our InfinityFlow analysis (Fig. 2A). Because T1 and T2 neutrophils were transcriptionally identified as immature and mature, respectively, in our scRNAseq data (Fig. 1D), we next evaluated CD101 expression, which separates immature neutrophils from mature neutrophils ([14]). Cluster 1 exhibited a continuum of CD101 expression (fig. S4B), suggesting that CD101 can be used to distinguish T1 and T2 neutrophils within the dcTRAIL-R1$^-$ population. Using CD101 and dcTRAIL-R1 to identify the different neutrophil types by flow cytometry (Fig. 2E), we isolated putative T1, T2, and T3 neutrophils and discovered that putative T1 neutrophils had

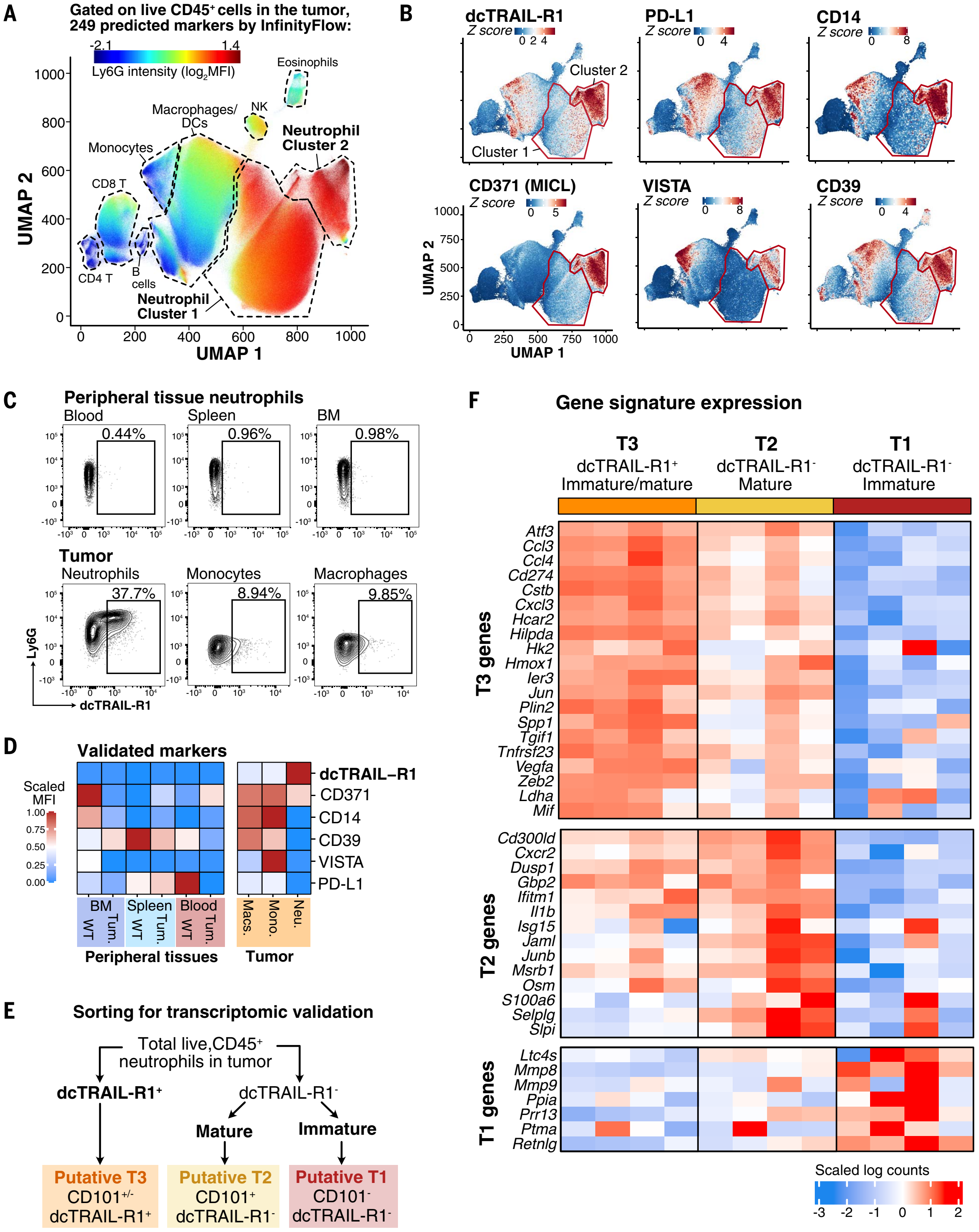

**Fig. 2. Combinatorial CD101 and dcTRAIL-R1 expression identifies T1, T2, and T3 neutrophils.** (**A**) UMAP projection of live CD45$^+$ immune cells within the PDAC tumor reveals two clusters of neutrophils. High-parameter flow cytometry was performed on single-cell suspensions of pooled tumors (*n* = 10 biological replicates) using the LEGENDScreen panel (BioLegend). Live CD45$^+$ well-compensated FCS were first analyzed and then exported out for analysis using the InfinityFlow package in R. UMAP shows Ly6G expression intensity imputed by InfinityFlow from high (red) to low (blue). Clusters are annotated by canonical surface marker expression (see also fig. S3B). (**B**) Neutrophil cluster 2 has increased expression of immunosuppressive and/or immunomodulatory surface markers compared with cluster 1. Surface marker expression intensities are shown for curated surface markers (clockwise): dcTRAIL-R1, PD-L1, CD14, CD371, VISTA, and CD39. Data are represented as a *Z* score based on predicted log$_2$ mean fluorescence intensity (MFI) from high (red) to low (blue) (see also fig. S3C). (**C**) dcTRAIL-R1 expression marks and is restricted to a separate population of tumor-infiltrating neutrophils. Representative contour flow cytometry plots (top) show dcTRAIL-R1 expression against Ly6G expression in the tumor for indicated cell populations. (**D**) Heatmap shows scaled MFI for markers in (B), scaled between 0 and 1 across all populations, with 0 being the lowest MFI. Populations were analyzed by flow cytometry, in which total neutrophils were gated as CD11b$^+$CD115$^-$Ly6G$^+$ in the BM, spleen, blood, and tumor. Tumor macrophages (CD11b$^+$Gr-1$^-$F4/80$^{hi}$MHCII$^{hi}$) and monocytes (CD11b$^+$Ly6G$^-$Ly6C$^{hi}$) were gated accordingly (see also fig. S3D). (**E**) Proposed gating strategy to isolate T1, T2, and T3 neutrophils by dcTRAIL-R1 and CD101 expression from the tumor. (**F**) Sorted dcTRAIL-R1$^+$ tumor neutrophils have the highest expression of the T3 transcriptional signature. Heatmap shows scaled Nanostring gene counts (normalized against internal positive controls and housekeeping genes) for T1 (*n* = 4), T2 (*n* = 4). and T3 (*n* = 4) neutrophils sorted according to (D). Numbers represent the biological replicates across two independent experiments. Genes belonging to either the T1, T2, or T3 transcriptional signature are indicated (see also fig. S4D).

a toroidal nuclear morphology resembling immature neutrophils from the BM (fig. S4C). Putative T2 neutrophils had hypersegmented nuclei similar to those of mature BM neutrophils (fig. S4C), whereas putative T3 neutrophils contained cells with hypersegmented or toroidal nuclear morphology (fig. S4C), congruent with our findings that T3 neutrophils are reprogrammed from both immature and mature neutrophils. Next, we found that dcTRAIL-R1$^+$ neutrophils showed the highest expression of T3 genes (table S3), whereas the dcTRAIL-R1$^-$CD101$^-$ and dcTRAIL-R1$^-$CD101$^+$ populations were strongly enriched for genes associated with T1 and T2 neutrophils, respectively (Fig. 2F and fig. S4D). Finally, all three neutrophil populations were identified in all experimental tumor models examined (fig. S4E), and the frequencies of the T1 to T3 populations in PDAC as determined by scRNAseq were comparable to the median frequencies of putative T1 to T3 populations isolated by flow cytometry (fig. S4, E and F). Thus, dcTRAIL-R1 and CD101 expression phenotypically divides tumor neutrophils into three distinct populations and successfully recapitulates the T1 to T3 populations defined in our transcriptomic and epigenetic approaches.

### Spatial compartmentalization of neutrophils in tumors

Spatial mapping of immune microenvironments in tumors has been highly informative by providing insights into their diversity and functionality on the basis of their localization within the tumor (*33*). To gain a better understanding of how tumor neutrophils are affected by their localization in the tumor, we first investigated possible functional differences between the three tumor neutrophil subsets by performing gene ontology (GO) analysis on differentially expressed T1, T2, and T3 genes (table S4). T1 neutrophils were enriched for pathways relating to transcription and translation (including genes governing ribosomal biogenesis such as *Npm1*) and oxidative phosphorylation (proton membrane transport) (Fig. 3A), which is consistent with the immature phenotype of T1 neutrophils (*14*). T2 neutrophils were enriched in pathways related to transcriptional regulation, amide and reactive oxygen species metabolism, and immune responses, as well as type I interferon genes, including *Ifit1*, *Ifit2*, *Ifit3*, and *Isg15* (Fig. 3B), which likely reflects neutrophil activation upon tumor infiltration. Finally, T3 neutrophils featured pathways of cell stress and survival, including response to hypoxia, oxidative stress, and glycolysis, (Fig. 3C), suggesting adaptation to the tumor environment. T3 neutrophils were also enriched for angiogenic genes, including *Vegfa*, *Thbs1* (*34*), and *Lgals3* (*35*), which, when combined, is suggestive of a strong protumoral role.

We next characterized how neutrophils with distinct transcriptional states would interact with the neighboring tumor microenvironment. Using 4′,6-diamidino-2-phenylindole (DAPI) and pan-cytokeratin (panCK) costaining, we noted that our orthotopic tumors were mainly composed of tumor cell regions (PanCK$^{high}$DAPI$^{high}$), fibrotic and/or necrotic regions (panCK$^{high}$DAPI$^{-/low}$), and sparse stromal regions along the edges (panCK$^{-/low}$DAPI$^{high}$) (fig. S5, A and B). We performed spatial transcriptomics on four cryosections of three different PDAC tumor samples (Fig. 3D). As expected, necrotic regions with low numbers of DAPI$^+$ cells contained low-quality counts, which were manually annotated and filtered to mitigate RNA contamination from nearby spots and to improve downstream analyses (fig. S5, C and D). We next assessed the tumor architecture by using BayesSpace (*36*) to identify transcriptionally similar neighborhoods within the tumor (fig. S5E). Clustering and UMAP embedding revealed that 10 clusters were shared across all four sections (fig. S5E). Indicative of the complexity of the tumor environment, the distributions of spatial clusters identified were different in the two cryosections [regions of interest 1 and 2 (ROI1 and ROI2)] taken from different regions of the same tumor (fig. S5E). Each spatial cluster had specific functional pathways associated with their distribution (fig. S5F). For example, regions enriched for pathways related to epithelial-to-mesenchymal transition (EMT, clusters 1 and 10), typically associated with the invasive tumor front (*37*), were present closer to the tumor periphery, whereas regions associated with hypoxia (cluster 6) and cell cycle progression ($G_2$-M checkpoint, cluster 2) were located close to the core of the tumor (fig. S5, E and F).

Using Cell2location (*38*) with a pre-annotated scRNAseq dataset (fig. S6A) allowed us to map the full transcriptional signature of each cell cluster within the tumor and estimate cell type abundances within each spot. To ensure the accuracy of neutrophil assigned spots, we ascertained the presence of Ly6G immunofluorescence staining falling within the spot as a selection cutoff (fig. S6B). Cell2location revealed that T1, T2, and T3 neutrophils mapped to different regions within the tumor (Fig. 3E), with visualization of T3 enriched spots on the UMAP embedding indicating that T3 neutrophils had the highest enrichment in spatial cluster 6, which was associated with hypoxia (Fig. 3F). T3 neutrophils were also observed to be mostly distributed adjacent to PanCK$^{high}$DAPI$^{-/low}$ necrotic zones (Fig. 3G), consistent with their localization to cluster 6 (fig. S5E). By contrast, T1 neutrophils were highly enriched in the cluster 1 (EMT) and clusters 7 and 8 (IL-2 and STAT5 signaling, respectively) regions, whereas T2 neutrophils were mostly found in cluster 3 associated with p53 signaling (Fig. 3F). Both T1 and T2 annotated spots were generally localized closer to the tumor periphery compared with T3 neutrophils (Fig. 3G). Our data suggest that neutrophils are spatially organized within the tumor, and T3 neutrophils occupy a tumor niche that is distinct from that of T1 and T2 neutrophils.

### Reprogrammed neutrophils occupy a hypoxic and glycolytic tumor niche

Because T3, but not T1 or T2, neutrophils had transcriptional and epigenetic profiles that were enriched for the hypoxia, glycolysis, and angiogenesis pathways, we evaluated whether this was reflected in their localization to hypoxic, glycolytic, or angiogenic regions within the tumor, respectively. All spots within the tumor region were first scored for GO pathways corresponding to glycolysis (fig. S6C), hypoxia (fig. S6D), and angiogenesis (fig. S6E), with a 50th percentile cutoff used to determine low and high regions. We then determined the frequency of neutrophil-containing spots falling into low and high regions for each tumor neutrophil subset. T3 neutrophils were found at greater frequencies in high scoring regions for glycolysis (68.8 ± 19.7%), hypoxia (53.3 ± 4.65%), and angiogenesis (62.2 ± 14.2%) (Fig. 3H). By contrast, most T2 (fig. S6F) and T1 (fig. S6G) neutrophil-containing spots fell into regions with low glycolysis, hypoxia, and angiogenesis scores, indicating that partitioning of the neutrophil subsets potentially results from T3 neutrophils occupying a specific regional hypoxic and glycolytic tumor niche.

We next set out to validate these observations at single-cell resolution because the current Visium spatial transcriptomic resolution is limited to 55-μm spots. We used MACSima imaging cyclic staining (MICS) (Fig. 4A), in which iterative immunofluorescence staining and photobleaching allows for the evaluation of large numbers of antibody targets within the same tissue slice (*39*). Optimization was first performed to determine working markers within orthotopic pancreatic tumor tissues (fig. S7, A and B), given that MICS staining times were relatively short at 10 min. Testing revealed that CD29, Galectin-3, and CD44, which typically mark fibroblasts (*40*–*42*), displayed the greatest staining at peripheral stromal and desmoplastic (panCK$^{-/low}$DAPI$^{hi}$) regions (fig. S7C), whereas CD31 and CD105 marked vessels within the stromal and tumor region (panCK$^+$). CD105 was able to better resolve intratumoral vessels (fig. S7C), consistent with their role in marking tumor-associated endothelium (*43*). To identify hypoxic regions within the tumor, Hif1a, CD39, and CD73 staining was evaluated. CD73, an adenosine monophosphate ectoenzyme, has been found to be directly induced by hypoxia and Hif1a in cancer (*44*–*47*). Immunofluorescence analysis revealed diverse staining patterns of CD73 in both stromal and desmoplastic regions and tumor (panCK$^+$) regions (fig. S7C), resembling the spatial distribution of hypoxia gene signature scores observed in

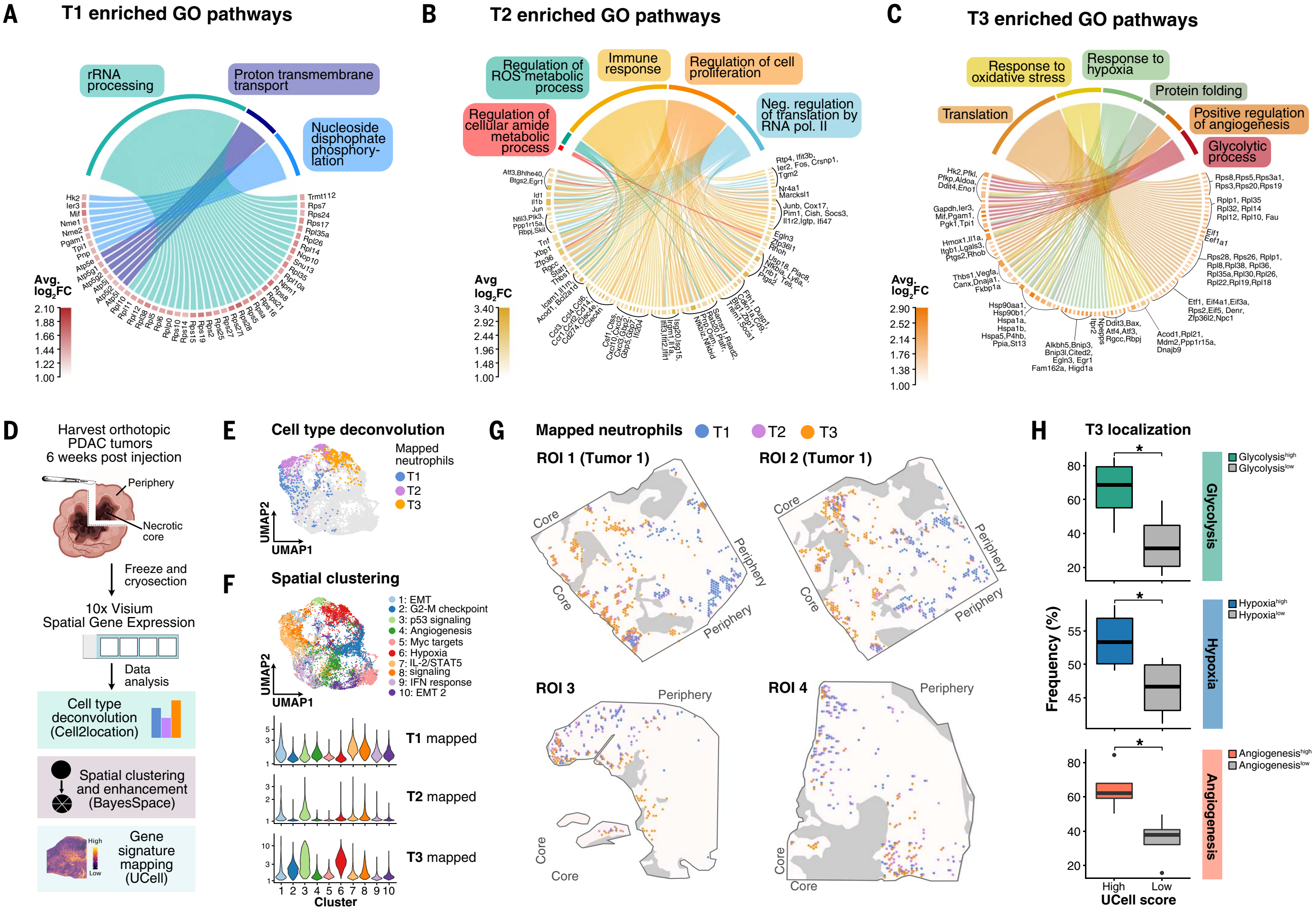

**Fig. 3. Spatial compartmentalization of T1, T2, and T3 neutrophils in the pancreatic tumor.** (**A**) Chord diagram showing differentially expressed genes (DEGs) in T1 neutrophils that are enriched for GO pathways linked to transcription and oxidative phosphorylation. (**B**) Chord diagram showing DEGs in T2 neutrophils that are enriched for GO pathways linked to metabolism and immune response. (**C**) Chord diagram showing DEGs in T3 neutrophils that are enriched for GO pathways linked to survival and angiogenesis. In (A) to (C), bars associated with each gene are colored by strength of fold change of differential expression and are sized based on the number of pathways with which it interacts (see also table S4 for DEG lists). (**D**) Spatial transcriptomic analysis workflow. PDAC tumors were isolated and cut into quarters, where the sharp edges denote the core facing regions, before flash-freezing. Fresh frozen PDAC tumors were sectioned and placed on 10X Visium slides containing spatially barcoded capture spots. After processing and sequencing, the data were clustered spatially (BayesSpace) and cell type deconvolution was performed (Cell2location). Gene signatures of various biological processes were then probed and mapped with the UCell package. (**E**) Tumor neutrophils localize to different spatial clusters. Projection of T1, T2, and T3 enriched spots identified by Cell2location on merged UMAP derived from BayeSpace enhanced clustering analysis of tumor sections ($n$ = 4 biological replicates). (**F**) Merged UMAP representation of spots of tumor sections were analyzed and color-coded according to BayesSpace-identified clusters (top). Violin plots show frequency of T1, T2, and T3 neutrophils enriched spots that map to each cluster (bottom). (**G**) Spatial mapping of T1, T2, and T3 neutrophils across tumor sections ($n$ = 4) by Cell2location. Black lines denote the outline of the section; gray colored areas indicated the excluded DAPI$^-$panCK$^{hi}$ regions annotated to be fibrotic and or necrotic. Spots are filtered based on Ly6G$^+$ staining (see also fig. S6B). (**H**) Quantification of percentages of deconvoluted T3 neutrophil-enriched spots falling into high- or low-scoring spots for GO ontology pathways: glycolysis (GO: 0061621), hypoxia (GO: 001666), and angiogenesis (GO: 0045766). Center line of boxplots show median, box hinges represent 25th and 75th percentiles, and whiskers extend to minimum and maximum values. *$P$ < 0.05 by one-tailed $t$ test.

our 10X Visium analysis (fig. S6B). By contrast, Hif1a did not stain within the MICS time frame, whereas CD39 mostly identified vessels (fig. S7C). Similarly, GLUT1 (glucose transporter 1) staining showed regional restriction (fig. S7C) similar to glycolysis signature scores (fig. S6B). Thus, CD73 and GLUT1 representative staining was used to define the hypoxic and glycolytic tumor niche. T1, T2, and T3 neutrophils were identified by staining for Ly6G, CD101, and dcTRAIL-R1, respectively, based on our flow cytometric strategy (Fig. 2D), and were successfully annotated in both confocal (fig. S7D) and MICS (fig. S7E).

We performed MICS for five different ROIs across two different orthotopic pancreatic tumors at 4 to 6 weeks after injection. ROIs were selected to unequivocally cover an entire region from the left to right margin encompassing the core of the tumor (fig. S8, A and B), and we observed staining across the full panel for all markers surveyed (fig. S9). We next specifically evaluated staining for the tumor vasculature (CD105), hypoxia (CD73), and glycolysis (GLUT1) across all five ROIs (Fig. 4C and fig. S8, A and B). CD105$^+$ blood vessels were present as a diffuse network scattered throughout the tumor (Fig. 4C and fig. S8, A and B). A gradient of CD73 staining was apparent throughout the tumor, whereas GLUT1 staining was more tightly localized; however, GLUT1$^{hi}$ areas strongly colocalized with CD73$^{hi}$ regions marking a distinct hypoxic and glycolytic niche (Fig.

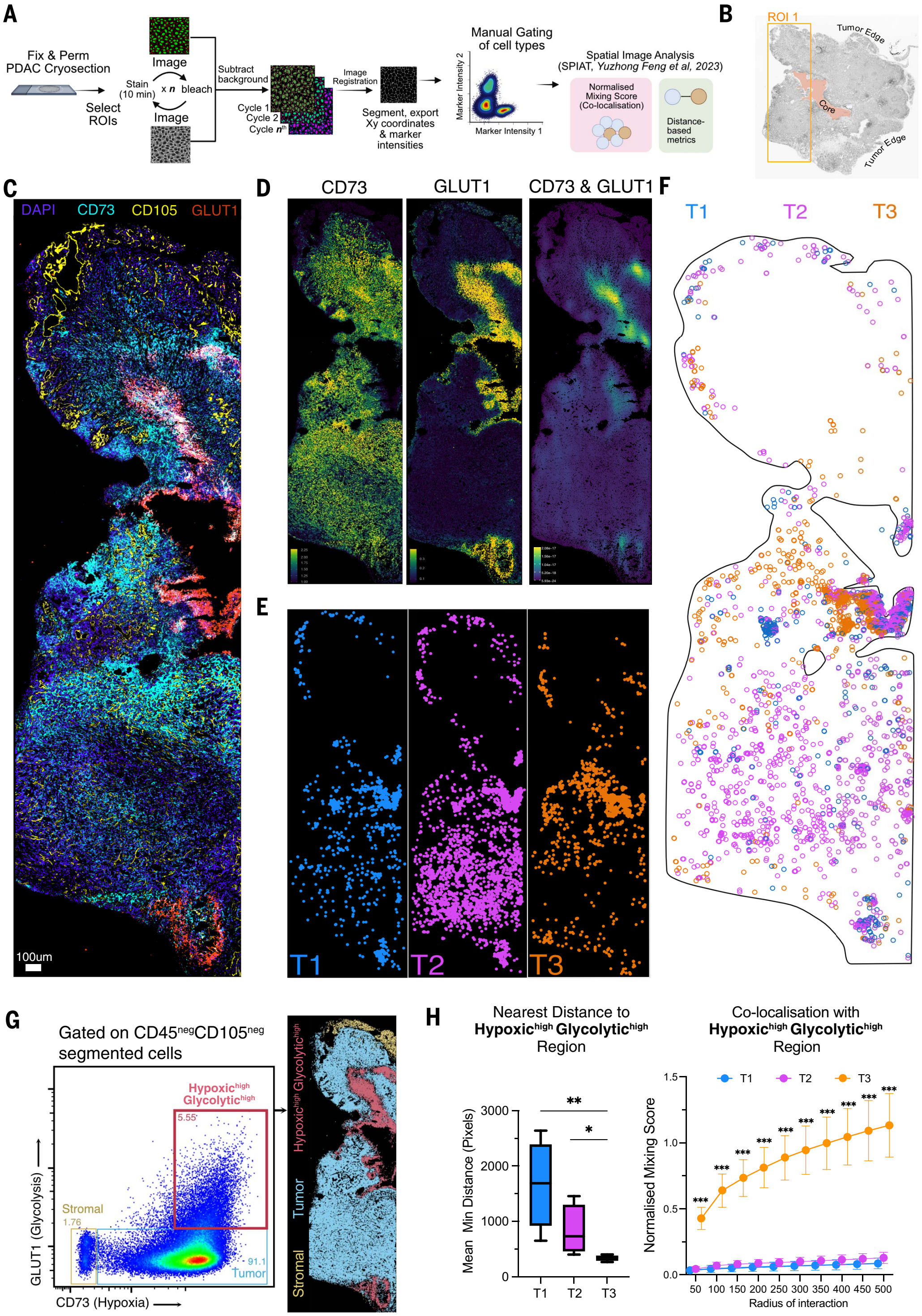

**Fig. 4. T3 neutrophils occupy a hypoxic-glycolytic niche in pancreatic tumors.** (**A**) Workflow diagram of multiplexed imaging using MICS technology. Cryosections of halved PDAC tumors were placed on slides, fixed, and permeabilized before ROI selection with DAPI staining. Sections were stained for 10 min per cycle containing antibodies in FITC, PE, and APC. After scanning, sections were photobleached and scanned to subtract background signals. After imaging the desired cycles, images were registered, segmented, and exported for conventional flow cytometric annotation of cell types, which were further used for spatial statistical analysis with SPIAT. (**B**) Tumor pictograph showing ROI1 selection area. (**C**) Immunofluorescent image of ROI1 with indicated stain markers of respective tumor regions. Scale bar, 100 μm. (**D**) Left, Expression marker intensity map of CD73 and GLUT1. Right, Coexpression plot of CD73 and GLUT1 marker intensities. (**E**) Spatial mapping of each annotated tumor neutrophil subsets in ROI1. (**F**) Comapping of neutrophil subsets in ROI1. (**G**) Left, Gating strategy of CD45$^-$ CD105$^-$ tumor regions demarcated by CD73 and GLUT1. Right, Mapped gated regions on segmented data of ROI1. (**H**) Spatial statistical analysis of segmented tumor neutrophils (*n* = 5 biological replicates). Left, Average minimum distance of each segmented neutrophil subset to hypoxic$^{high}$glycolytic$^{high}$ regions. Center line of boxplots show median, box hinges represent 25th and 75th percentiles, and whiskers extend to minimum and maximum values. *$P < 0.05$, **$P < 0.01$ by Mann-Whitney *U* test. Right, Colocalization of tumor neutrophils with hypoxic$^{high}$glycolytic$^{high}$ regions measured using a normalized mixing score for each radius of interaction. Dots represent mean across five replicates. Error bars indicate SEM. ***$P < 0.001$ by Mann-Whitney test, corrected for multiple comparisons with a false discovery rate (FDR) of 1% using the two-stage step up (Benjamini, Krieger, and Yekutieli) method.

4D and fig. S8, A and B). Annotation of T1 (Ly6G$^+$CD101$^-$dcTRAIL-R1$^-$) and T2 (Ly6G$^+$CD101$^+$dcTRAIL-R1$^-$) neutrophils (fig. S8C) revealed that they were distributed throughout the tumor parenchyma in two different patterns reflective of their likely routes into the tumor: bordering the tumor edges in CD73$^-$ stromal regions or diffused throughout GLUT1$^-$CD73$^+$ regions, both of which contained a substantial network of CD105$^+$ vessels (Fig. 4E and fig. S8, A and B). By contrast, T3 (Ly6G$^+$CD101$^{-/+}$dcTRAIL-R1$^+$) neutrophils across all ROIs were more likely to cluster together at the CD73$^{hi}$GLUT1$^{hi}$ hypoxic and glycolytic niche (Fig. 4E), thus giving rise to a clear spatial segregation of the three neutrophil populations, as suggested by our 10X Visium analysis (Fig. 4F and fig. S8, A and B).

Next, we agnostically quantified the three neutrophil subgroups' relative locations within the tumor. Using marker intensities on segmented cells, we excluded CD45$^+$ immune cells and CD105$^+$ endothelial cells and subdivided the remaining cells into three distinct regions: the stromal niche (CD73$^-$GLUT1$^-$), the tumor parenchyma niche (CD73$^+$GLUT1$^-$), and the hypoxic$^{high}$glycolytic$^{high}$ tumor niche

($CD73^{hi}GLUT1^{hi}$) (Fig. 4G and fig. S8C). In all five ROIs, T3 neutrophils had the shortest average minimum distance to the $hypoxic^{high}glycolytic^{high}$ niche compared with T1 and T2 neutrophils (Fig. 4H). We then assessed normalized mixing scores, which quantify the proportion of direct touches between the target regions and reference neutrophil cells (target-reference) against reference-reference interactions ([48]). T3 neutrophils had the greatest mixing scores within $hypoxic^{high}glycolytic^{high}$ tumor regions, which was conserved with each radius of area investigated (Fig. 4H). Scores for the stromal region showed a trend for highest scores in T1, followed by T2, with T3 being minimally detected within the stroma (fig. S8D). Finally, T2 neutrophils trended toward higher proportions of interspersion within the tumor parenchyma compared with T1 and T3 neutrophils (fig. S8D). These observations suggest that T1 and T2 neutrophils are mostly located away from the $hypoxic^{high}glycolytic^{high}$ regions, in contrast to T3 neutrophils. Therefore, our spatial data imply that T3 neutrophils likely migrate into and occupy the specialized hypoxic-glycolytic tumor niche. This is consistent with our finding that transcription factor regulons enriched in T3 neutrophils (Fig. 1H) include those up-regulated in response to hypoxia (e.g., *Hif1a* and *Bhlhe40*) and to metabolic and ER stress (e.g., *Atf4*, *Ddit3*, *Atf3*, and *Nfe2l2*). Thus, epigenetic and transcriptional up-regulation of these pathways in T3 neutrophils could confer an added survival advantage within these tumor microenvironments. Collectively, our data provide a spatial representation by which tumor neutrophils converge upon the occupancy of a specialized tumor niche upon reprogramming.

## Deterministic reprogramming of neutrophils in the tumor

Because both mature and immature neutrophils were predicted to give rise to T3 neutrophils inside the tumor, we examined the impact of the maturation state on the acquisition of the T3 signature. We first isolated immature and mature neutrophils from WT mice and cultured them with tumor conditioned medium (TCM), which allowed us to mimic the infiltration of immature and mature neutrophils into the tumor microenvironment (Fig. 5A). We then measured up-regulation of dcTRAIL-R1 on cultured neutrophils across multiple time points as a proxy to estimate the acquisition of the T3 profile (Fig. 5A). After 3 days, a substantial proportion of BM immature and mature neutrophils cultured in TCM were dcTRAIL-R1$^+$, but not those cultured in control media [i.e., complete Dulbecco's modified Eagle's medium (cDMEM)] (Fig. 5A). Specifically, exposure to TCM could trigger dcTRAIL-R1 expression 24 hours into culture and prolonged survival up to 3 days compared with culture in cDMEM (fig. S10, A and B). We obtained similar results regardless of tissue origin or maturation state, such that neutrophils isolated from the BM, spleen, and circulation cultured in TCM all exhibited dcTRAIL-R1 up-regulation and concurrent increased survival (Fig. 5B and fig. S10, A and B). Furthermore, exposure to TCM induced the up-regulation of the T3 gene signature in immature and mature neutrophils (Fig. 5C). We then assessed whether culture in hypoxic conditions would enhance neutrophil survival or dcTRAIL-R1 up-regulation of WT neutrophils. Culture in hypoxic conditions slightly augmented neutrophil survival in vitro, especially for mature neutrophils (fig. S10C), but did not induce dcTRAIL-R1 expression (fig. S10D), indicating that hypoxic conditions are not the main driver of T3 reprogramming. Adoptive transfer of CD45.1$^+$ immature and mature neutrophils into tumor-bearing mice (Fig. 5D) further confirmed that exposure to the tumor microenvironment was necessary for the up-regulation of dcTRAIL-R1 (Fig. 5E), and dcTRAIL-R1 up-regulation in vivo followed the same kinetics as in vitro (Fig. 5F and fig. S11A). Therefore, exposure to tumor-derived stimuli supports extended survival and the acquisition of the T3 phenotype in WT neutrophils.

Both TCM-cultured immature and mature neutrophils up-regulated dcTRAIL-R1 expression and the T3 gene signature to an equal degree, indicating that immature neutrophils could be reprogrammed directly into T3 neutrophils (Fig. 5, A and C). RNA velocity analysis suggested that this occurs in a stepwise fashion as immature neutrophils transit into T1 neutrophils and subsequently differentiate into T3 neutrophils (Fig. 1E). As expected, transfer of CD45.1$^+$ immature neutrophils resulted in the appearance of dcTRAIL-R1$^-$CD101$^-$ T1 neutrophils within the tumor 1 day after transfer (fig. S11B). By contrast, only dcTRAIL-R1$^-$CD101$^+$ T2 neutrophils, not T1 neutrophils, were observed in the tumor with CD45.1$^+$ mature neutrophil adoptive transfer (fig. S11B). Both T1 and T2 populations derived from transferred cells were undetected after 3 days within the tumor because most of these transferred cells had completed their reprogramming into dcTRAIL-R1$^+$ T3 neutrophils (fig. S11C). We further corroborated the transitory nature of T1 and T2 subsets by in vitro culture (fig. S11, D and E). Isolated T1 and T2 neutrophils up-regulated dcTRAIL-R1 expression after 24 hours in culture. Unlike tumor-naïve neutrophils, dcTRAIL-R1 up-regulation was independent of the culture medium used for both T1 (fig. S11F) and T2 (fig. S11G) neutrophils. Therefore, T1 and T2 neutrophils reflect immature and mature neutrophil populations captured in the process of T3 differentiation and thus do not require any further input from tumor soluble factors. Our findings suggest a deterministic program within neutrophils that enables them to acquire the T3 phenotype independent of their maturation stage.

## T3 neutrophils are long-lived, terminal effectors within the tumor microenvironment

To better understand the temporal regulation of neutrophil differentiation into the T3 state within the tumor microenvironment in vivo, we administered 5-bromo-2′-deoxyuridine (BrdU) intravenously at selected time points before harvest, pulse-labeling all proliferating neutrophil precursors (Fig. 5G). This approach defines a time stamp at the point of labeling, allowing us to evaluate all time points simultaneously at the time of harvest, thereby minimizing batch effects. Modeling the disappearance rate from the peak of BrdU$^+$ signal (fig. S12, A and B) and incorporating the entire temporal interval measured allowed the prediction of neutrophil half-life and lifespans (fig. S12C), reflecting their dwell time within each tissue compartment (Fig. 5G).

The earliest peak of BrdU$^+$ neutrophils was observed in the BM and spleen, because of active granulopoiesis within these organs in the tumor-bearing state, whereas recruitment of BrdU-labeled neutrophils into the blood and subsequently the tumor placed their peak of recruitment at ~4 to 5 days after labeling (Fig. 5G). Because the dwell times of neutrophils in the BM and spleen are complicated by continual neutrophil production, we focused our comparison between the blood and tumor neutrophils. Blood neutrophils had a half-life of 31.4 hours, reflecting an increased transit time in circulation compared with previously predicted times for WT blood neutrophils ([49]). Even so, tumor neutrophils had an even longer half-life [41.8 hours; 95% confidence interval (CI) = 39.6 to 46.6] and a predicted life span of 135 hours (up to 5.625 days; 95% CI = 126.5 to 142.4) (Fig. 5G and fig. S12, C and D), representing a marked extension of neutrophil life span within the tumor microenvironment. Compared with the unmarked BrdU$^-$ fraction, the proportion of BrdU$^+$ dcTRAIL-R1$^+$ neutrophils increased over time, surpassing baseline levels at day 6 after labeling (fig. S12, E and F). Newly recruited BrdU$^+$ tumor neutrophils already expressed dcTRAIL-R1 at 1 day after labeling (fig. S12E), suggesting that T3 reprogramming is initiated upon tumor entry. dcTRAIL-R1 expression steadily increased and was the highest in neutrophils at 15 days after labeling (Fig. 5, H and I), confirming that acquisition of the T3 phenotype was associated with their extended lifespans in vivo. Our results show that a notable increase in the duration of neutrophil half-life and residence in the tumor compared with those in nontumor tissues (fig. S12D), indicating that neutrophils can survive long enough within the tumor to undergo reprogramming and sustained persistence

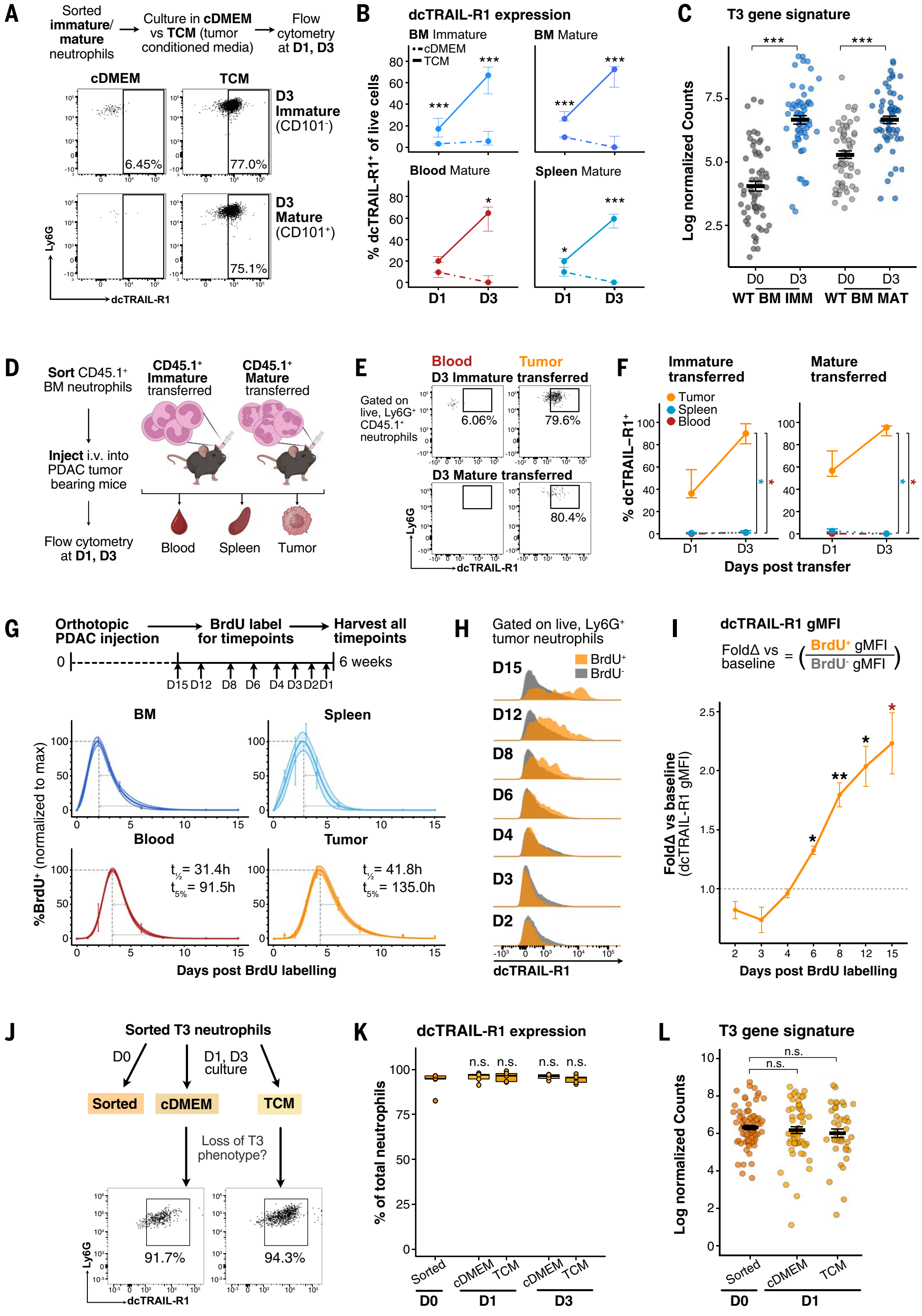

**Fig. 5. Reprogramming within the tumor environment results in long-lived, terminally differentiated T3 neutrophils.** (**A**) Experimental setup of in vitro culture of sorted neutrophils from WT mice in cDMEM versus TCM. Representative flow cytometry plots show dcTRAIL-R1 expression increases on sorted immature and mature WT neutrophils from the BM after 3 days of culture in TCM but not in cDMEM. (**B**) Neutrophils cultured in TCM up-regulate dcTRAIL-R1 over time. Line plots show the percentage of dcTRAIL-R1$^+$ cells gated as in (B), dots indicate the median, and error bars indicate Q1 and Q3 intervals for neutrophil subsets cultured in cDMEM (dotted line) and TCM (solid line) over 1 and 3 days. Each group contains the following number of samples: day 1 cDMEM: BM immature ($n = 8$), BM mature ($n = 8$), spleen mature ($n = 8$), blood mature ($n = 3$); day 1 TCM: BM immature ($n = 8$), BM mature ($n = 8$), spleen mature ($n = 8$), blood mature ($n = 5$); day 3 cDMEM: BM immature ($n = 10$), BM mature ($n = 10$), spleen mature ($n = 10$), and blood mature ($n = 4$); day 3 TCM: BM immature ($n = 10$), BM mature ($n = 10$), spleen mature ($n = 10$), blood mature ($n = 5$) performed across seven independent experiments. *$P < 0.05$, **$P < 0.01$, ***$P < 0.001$ by Mann-Whitney $U$ test. (**C**) Neutrophils cultured in TCM up-regulate the T3 gene signature. Scatter dot plots for T3 gene signature expression in BM immature (WT BM IMM) and mature (WT BM MAT) neutrophils that were freshly sorted (D0) or cultured for 3 days (D3) ($n = 3$ for all samples). Each dot denotes a single gene, lines denote the mean, and error bars indicate the SEM. ***$P < 0.001$ by Wilcoxon signed-rank test with Bonferonni's correction, with comparisons indicated on the graph. (**D**) Experimental setup for transfer of CD45.1$^+$ neutrophils into pancreatic tumor-bearing mice. Sorted WT BM immature and mature neutrophils were intravenously injected into WT PDAC tumor-bearing mice. At 1 and 3 days after transfer, CD45.1$^+$ neutrophils were evaluated within the blood, spleen, and tumor for dcTRAIL-R1 expression by flow cytometry. (**E**) Up-regulation of dcTRAIL-R1 expression was restricted to the tumor. Representative flow plots show dcTRAIL-R1 expression present on transferred CD45.1$^+$ immature and mature neutrophils present in the blood or tumor at 3 days after transfer. (**F**) Line plots show proportion of WT BM CD45.1$^+$ immature ($n = 4$ at day 1 and $n = 3$ at day 3) or mature neutrophils ($n = 3$ at both time points) expressing dcTRAIL-R1 performed across two independent experiments. Each dot denotes a single gene, lines denote the mean, and error bars indicate SEM. *$P < 0.05$ by Kruskal-Wallis test with Dunn's post test. (**G**) Experimental setup for BrdU pulse labeling in tumor-bearing mice. WT mice received orthotopic injection of the PDAC cells, and the tumor was allowed to grow. At days 15 ($n = 4$), 12 ($n = 4$), 8 ($n = 5$), 6 ($n = 3$), 4 ($n = 4$), 3 ($n = 4$), 2 ($n = 3$), and 1 ($n = 4$) before the harvest, mice were injected with BrdU, thus labeling proliferating neutrophil precursors within the BM and spleen. Data were collected across three independent experiments. At day 42 (6 weeks) after injection, mice were sacrificed and BrdU$^+$ neutrophils within the BM, spleen, blood, and tumor were quantified. BrdU percentages at all time points were then normalized to the maximal BrdU$^+$ percentage value for each tissue, which was set to 100%. Dots represent mean expression, with error bars denoting 95% CIs.

A mathematical model capturing the full temporal window was fitted to estimate half-life ($t_{1/2}$) and life span ($t_{5\%}$) for each organ, denoted on each plot in hours (see also fig. S12C and the materials and methods). (**H**) BrdU labeled neutrophils up-regulate dcTRAIL-R1 over time. Histograms show geometric MFI (gMFI) of dcTRAIL-R1 within BrdU$^+$ (orange) and BrdU$^-$ (gray) neutrophils at days 2, 3, 4, 6, 8, 12, and 15 after BrdU labeling. (**I**) Quantification of gMFI in (H). Line plots show fold change of dcTRAIL-R1 gMFI of BrdU$^+$ against BrdU$^-$ neutrophils. BrdU$^-$ neutrophils served as a measure of baseline dcTRAIL-R1 gMFI within the tumor. Each dot denotes the mean, with error bars indicating SEM. $^*P < 0.05$, $^{**}P < 0.01$ by Mann-Whitney *U* test, one-tailed, alternative = "greater." (**J**) Experimental setup of in vitro culture of sorted T3 neutrophils from PDAC mice in cDMEM or TCM at 1 or 3 days. Representative flow cytometry plots show that dcTRAIL-R1 expression is retained on T3 neutrophils after 1 day of culture in both cDMEM and TCM. (**K**) Boxplots show quantification of frequency of dcTRAIL-R1$^+$ neutrophils ($n = 5$ each performed across three independent experiments) in (I). Each dot represents one biological replicate, center line of boxplots show median, box hinges represent 25th and 75th percentiles, and whiskers extend to minimum and maximum values. $P$ = n.s. (not significant) by Kruskal-Wallis followed by many-to-one *U* test comparing against the D0 time point. (**L**) T3 neutrophils cultured overnight do not down-regulate the T3 gene signature. Scatter dot plots for T3 gene signatures in sorted, cDMEM-, or TCM-cultured neutrophils ($n = 3$ each). Each dot denotes a single gene, lines denote the mean, and error bars indicate SEM. $P$ = n.s. by Kruskal-Wallis followed by Dunn's post test.

within the tumor as long-lived dcTRAIL-R1$^+$ T3 neutrophils.

To determine whether the T3 state is transitory or is stably maintained once it has been acquired, we isolated and cultured T3 neutrophils overnight and up to 3 days in the presence or absence of TCM (Fig. 5J). Survival of T3 neutrophils in culture was not affected by the medium type (fig. S12G), and dcTRAIL-R1 expression was maintained despite the absence of tumor-derived factors (Fig. 5K), with expression levels comparable to freshly isolated T3 neutrophils at both time points (fig. S12H). Additionally, T3 neutrophils did not down-regulate their gene signature in culture (Fig. 5L). This in vitro evidence indicates that once neutrophils have been reprogrammed into T3 neutrophils, they do not revert their phenotype in the absence of supportive tumor factors and they represent the terminally differentiated neutrophil population within the tumor.

## T3 neutrophils are pro-angiogenic and promote tumor growth

Prior studies have identified key roles for neutrophils in tumor progression, especially through the promotion of tumor angiogenesis (*50*–*52*). We therefore sought to determine the functional specialization of T1 to T3 neutrophils in promoting tumor growth. Given their phenotypic stability, distribution near angiogenic regions, and the expression of a pro-angiogenic transcriptional signature (Fig. 3C), we speculated that T3 neutrophils promoted angiogenesis from their hypoxic-glycolytic niche to support continual tumor growth. By contrast, we anticipated that the transient T1 and T2 neutrophil states would not yet feature pro-angiogenic ability. T3 neutrophils had the highest transcript (Fig. 6A) and protein expression (Fig. 6, B and C) of *Vegfa* (vascular endothelial growth factor a) compared with the other neutrophil subsets in the tumor and periphery. We then evaluated whether T3 neutrophils had a greater capacity to induce blood vessel formation in vivo using a modified Matrigel plug assay and measured angiogenesis by the rate of vascular flow measured by Doppler imaging (*53*) (fig. S13A). Matrigel plugs co-injected with T3 neutrophils showed the greatest flux intensity compared with control WT BM neutrophil plugs within the same mouse (fig. S13B), and this increase in vascularization, although modest, was consistent across all mice observed in the assay (fig. S13C). By contrast, co-injection of T1 and T2 neutrophils did not enhance vascular flow (fig. S13, B and C), indicating that the T3 population contains the most potent angiogenic ability (Fig. 3C).

The tumor triggers angiogenesis to maintain the supply of oxygen and other nutrients to the core of the tumor to sustain continual growth (*54*). To test whether T3 neutrophils residing in their hypoxic-glycolytic niche at the tumor core support this angiogenic switch, we modified our PDAC model by implanting PDAC tumors subcutaneously to enable longitudinal tumor size measurements. We then assessed whether injection of neutrophils within the tumor affected their subsequent growth (Fig. 6D). PDAC cells co-injected with T3 neutrophils formed tumors that grew rapidly (Fig. 6D), whereas co-injection with other neutrophil types had little influence on tumor growth. T3-co-injected tumors had a 100% tumor growth rate (Fig. 6E, as evaluated in fig. S13D) and had the greatest mass at the end point (Fig. 6F). T2-co-injected tumors showed the lowest tumor incidence rates (5 of 12) (Fig. 6F), suggestive of increased tumor rejection and consistent with the expression of proinflammatory genes in T2 neutrophils detected in our scRNAseq dataset (Fig. 3B). T3-co-injected tumors continued to grow rapidly for up to 3 weeks after the last injection of neutrophils, suggesting that even after their disappearance, transferred T3 neutrophils generated long-lasting effects that sustained this accelerated growth rate. Neutralization of VEGFα in our model resulted in the reduction of growth in T3-co-injected tumors, but had no impact on the growth of WT BM mature (WTBM MAT)–co-injected tumors (Fig. 6G). To determine whether this growth enhancement was due to increased angiogenesis driven by T3 neutrophils, we optically cleared T3- and WTBM MAT–co-injected tumors (fig. S13E) and visualized the intratumoral three-dimensional (3D) vessel network through CD31 staining (Fig. 6H). T3-co-injected tumors had greater CD31 staining density toward the tumor core (Fig. 6H and movie S1), whereas the vessel network in WTBM MAT–co-injected controls showed greater distribution along the tumor edges (Fig. 6H and movie S2). Normalization for tumor size revealed that both T3 and WTBM MAT–co-injected tumors had similar densities of CD31$^+$ blood vessels (fig. S13F) but substantially differed in their distribution (Fig. 6I). Although T3 neutrophils were the highest expressors of *Vegfa* in the pancreatic tumor, *Vegfa* expression was also detected in macrophage populations (fig. S13G), indicating that neutrophils may not be the sole pro-angiogenic contributor for tumor growth support. Nonetheless, blockade of T3 neutrophils with an anti–dcTRAIL-R1 antibody decreased tumor growth in T3-co-injected tumors compared with isotype controls (Fig. 6J), indicating that T3 neutrophils are the predominant cells responsible for increasing the tumor growth rate, most likely through vascular remodeling.

## Evidence for conserved neutrophil reprogramming across tumor types and human PDAC

Phenotypic differences in tumor-infiltrating neutrophils have been observed across mouse and human cancers, and multiple subsets have been characterized by differential surface marker or transcriptome expression (*6*–*13*). Whether such neutrophil profiles are conserved across tumor types and species remains unclear. We therefore assessed whether T1 to T3 neutrophil states can be detected in previously published mouse cancer scRNAseq datasets containing annotated neutrophils (*11*, *13*). We projected these datasets onto a reference UMAP embedding, mapping each cell on the same UMAP space as our dataset (fig. S14A). As in the PDAC model, neutrophils within Lewis lung carcinoma tumors (*13*) could be assigned to the T1 to T3 states, whereas spleens from WT or tumor-bearing mice mostly contained nontumor neutrophil clusters (fig. S14B). An intermediate neutrophil subset identified in cancer-bearing individuals [PMN2 in (*13*)] was enriched in the preNeu and IMM 1 and 2 clusters (fig. S14C), whereas T1 to T3 clusters scored highly for the tumor-specific neutrophils (PMN3; fig. S14D). Similarly, reanalysis of a different scRNAseq dataset showed that neutrophils from their KP1.9 tumor-bearing lung model (*11*) mapped as T1 to T3 clusters, whereas the normal lung

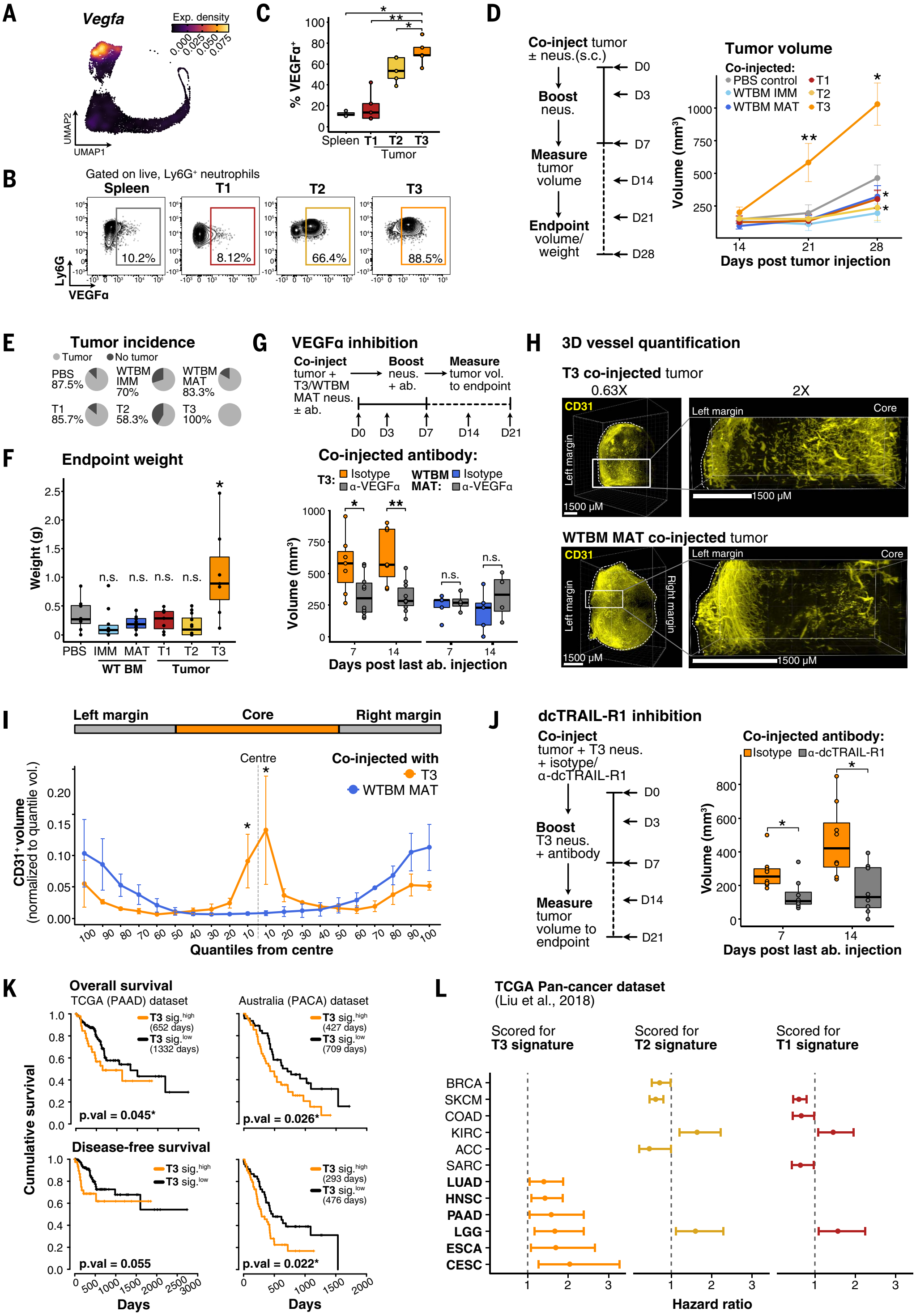

**Fig. 6. Protumoral T3 neutrophils promote tumor growth and associate with poorer patient outcomes.** (**A**) T3 neutrophils have the highest expression of *Vegfa* transcripts. UMAP projection of total neutrophils in BM, spleen, blood, and tumor show expression density of *Vegfa*. (**B**) T3 neutrophils have the highest expression of VEGFα. Representative flow plots show intracellular VEGFα protein staining in neutrophils from the spleen ($n = 3$) and T1, T2, and T3 neutrophils ($n = 5$ biological replicates) in the pancreatic tumor across two independent experiments. (**C**) Boxplots quantify VEGFα expression as shown in (B). Each dot represents one biological replicate, center line of boxplots show median, box hinges represent 25th and 75th percentiles, and whiskers extend to minimum and maximum values. $*P < 0.05$, $**P < 0.01$ by Kruskal-Wallis followed by many-to-one $U$ test comparing against T3 neutrophils. (**D**) T3 neutrophils promote rapid tumor growth. Schematic of experimental setup to determine the ability of neutrophils to promote tumor growth in vivo. Equal numbers of neutrophils and PDAC cells were mixed in Matrigel before subcutaneous injection into the right flank. Neutrophils in the tumor was boosted on day 3 (D3) and D7 by direct subcutaneous injection into the visible matrigel plug–tumor. Tumor growth was measured by calipers weekly until the day 28 end point. Line plots show volume of measured subcutaneous tumors co-injected with PBS ($n = 8$), WT BM immature (WTBM IMM, $n = 10$), WT BM mature (WTBM MAT, $n = 12$), and T1 ($n = 7$), T2 ($n = 12$), and T3 ($n = 7$) neutrophils. Data were collected across five independent experiments. Dots show means, with error bars indicating SEM over all three measurement time points. $*P < 0.05$, $**P < 0.01$ by Kruskal-Wallis test followed by many-to-one $U$ test comparing all other conditions to PBS co-injection. (**E**) Quantification of PDAC subcutaneous tumor incidence after neutrophil co-injection (see fig. S13D for quantification method). Piecharts show frequency of mice with tumors (light gray) or no tumor growth (dark gray) at day 28 end point in (D). (**F**) Tumors co-injected with T3 neutrophils had the biggest weights compared other conditions. Each dot represents one biological replicate, with boxplots showing median with IQR and whiskers indicating lowest and highest measurement. $P < 0.05*$ by Kruskal-Wallis test followed by many-to-one $U$ test comparing all other conditions with PBS co-injection. (**G**) Antibody neutralization of VEGFα reduces T3-mediated acceleration of tumor growth. Schematic of experimental setup with sorted T3 neutrophils are co-injected with PDAC tumor with anti-VEGFα targeting antibody ($n = 10$) or isotype control ($n = 7$). WT BM mature neutrophils were used as controls (anti-VEGFα targeting antibody, $n = 4$, isotype, $n = 5$). Data were collected across three independent experiments. Neutrophils were further injected on D3 and D7 with the corresponding antibody added, and tumor growth was measured at D14 and D21, 7 and 14 days after tumor injection. Boxplots show median tumor volume, where each dot represents one biological replicate, box hinges represent the interquartile range, and whiskers extend to the minimum and maximum values. $P < 0.05*$ by by Mann-Whitney $U$ test. (**H**) Visualization of CD31 vessels within T3 and WT BM MAT co-injected subcutaneous tumors. Subcutaneous tumors from (A) for T3 ($n = 3$) and WTBM MAT ($n = 3$ biological replicates) were dissected, optically cleared, and permeabilized, stained with anti-CD31 antibody, and imaged in 3D at 0.65×

(100% of total volume) and 2× (35% of total volume starting from midpoint) resolution. Data were collected across three independent experiments. Representative 3D immunofluorescence images show T3 (top, quarter) and WTBM MAT (bottom, whole) co-injected tumors, with tumor margins marked out in white dotted lines and indicated. (**I**) Subcutaneous PDAC tumors co-injected with T3 neutrophils have greater CD31 vessel density within the tumor core. Quantification of CD31 staining intensity at 2× resolution as in (E). CD31 staining was surfaced with a seedpoint of 16.2, and binned in 10% quantiles according to the distance from left or right margins toward the tumor core. To account for differences in tumor sizes, CD31 staining intensity was further normalized over total slice volume for each quantile. Line plots represent volume-normalized staining intensity, with dots representing the mean and errors bars indicating SEM for T3 (orange)– or WTBM MAT (gray)–co-injected tumors. *$P < 0.05$ by Mann-Whitney *U* test, one-tailed, alternative = "greater." (**J**) Antibody-mediated blockade of T3 neutrophils reduces their ability to promote rapid tumor growth. Schematic of experimental setup. Sorted T3 neutrophils were co-injected with PDAC tumor with anti–dcTRAIL-R1 targeting antibody ($n = 8$) or isotype control ($n = 8$). T3 neutrophils were further injected on D3 and D7 with the corresponding antibody added, and tumor growth was measured at D14 and D21, 7 and 14 days after tumor injection. Data were collected across four independent experiments. Boxplots show median tumor volume, with each point representing one biological replicate, box hinges represent the interquartile range with whiskers extending to minimum and maximum values. *$P < 0.05$ by Mann-Whitney *U* test. (**K**) The T3 neutrophil gene signature is associated with poorer patient OS and DFS in pancreatic cancer. Kaplan-Meier plots show OS (top) and DFS (bottom) for patients in the TCGA-PAAD and PACA-AU datasets. Patients were split into high and low expression of the T3 curated signature. Median OS and DFS survival are represented on the graph when available. Events are represented by vertical lines and were defined from days to death (from initial pathological diagnosis) or days to first event (from initial treatment, for TCGA, and from clinical disease-free diagnosis for PACA-AU). *$P < 0.05$ as calculated by log-rank test. (**L**) The T3 neutrophil gene signature is associated with poorer patient OS in a subset of solid human cancers. Each data set within the curated TCGA Pan Cancer dataset was scored for T1, T2, and T3 signatures (see also table S4). Forest plots show hazard ratio (HR) scores associated with patient OS that were significant ($P < 0.05$) by Cox proportional hazards test across all signatures. Dots indicate the calculated HR and whiskers indicate 95% CIs.

tissue was mostly enriched for mature neutrophils (fig. S14E). Likewise, neutrophil types identified as tumor-specific neutrophil clusters in this model [mN3-6 in (*11*)] corresponded to T1 to T3 clusters (fig. S14F), confirming that the tumor microenvironment induces a prototypical transcriptional trajectory that is deterministic in nature. By contrast, the signature of neutrophils from healthy lungs (*49*) was largely independent of tumor-induced transcriptional changes (fig. S14G). These data suggest that reprogramming of tumor neutrophils is conserved across different tumor types, and that T3 neutrophils represent terminal differentiated tumor neutrophils.

To examine cross-species conservation of the neutrophil tumoral trajectory found in mice, we investigated whether our neutrophil classification could account for the heterogeneity present in human tumors. We examined independent scRNAseq datasets (*55*, *56*) from two human PDAC cohorts (fig. S14, H and I) and mapped them to a simplified reference UMAP embedding through label transfer (fig. S14J). T2 and T3 neutrophils were amply labeled in both datasets, and a smaller cluster of T1 neutrophils was also identified (fig. S14, K and L). These tumor neutrophil subsets were predominantly enriched in the pancreatic tumor and not in adjacent normal pancreatic tissue (fig. S14K) or in the peripheral blood (fig. S14L). A pro-angiogenic neutrophil type expressing genes linked to hypoxia and glycolysis in one of these studies [referred to as TAN-1 (*56*)] strongly matched the T3 state in the murine tumor, indicative that our T3 classification can capture subsets independently identified to be protumoral (fig. S15A). Similarly, tumor neutrophil gene signatures derived from our mouse dataset (fig. S15B) were conserved in their ability to distinguish between human tumor neutrophils and showed strong specificity in identifying T1, T2, and T3 neutrophils within the tumor and not in the adjacent normal tissue (fig. S15B). Our findings suggest that tumor-induced reprogramming of neutrophils is conserved in humans.

Because T3 neutrophils promote the growth of pancreatic tumors, we hypothesized that the genetic signature associated with the T3 state might be predictive of pancreatic cancer outcomes in human patients. To test this, we performed survival analysis on two independent pancreatic cancer cohorts from The Cancer Genome Atlas (TCGA) and International Cancer Genome Consortium Pancreatic Cancer-Australia (PACA-AU) by scoring patients on the basis of high and low expression of each signature (see the materials and methods for scoring criteria). Patients with high expression of the T3 neutrophil signature had poorer overall survival (OS) across both datasets, with a median of 652 (TCGA) and 427 (PACA-AU) days, respectively (Fig. 6K), and this was independent of potential confounders such as patient gender, age, and tumor stage (table S5). Similarly, when disease-free survival (DFS, assessed as time to an adverse event from the initial treatment) was evaluated, patients with high T3 neutrophil signature expression had reduced DFS (Fig. 6M), with equal distribution of potential confounders across the two groups (table S6). When T1 and T2 signatures were considered, high T2 signature expression correlated with worse OS only in the TCGA dataset (fig. S15, C and D), but this was confounded by gender (table S5), whereas high T1 signature expression was associated with lower DFS only in the PACA-AU dataset (fig. S15, E and F). Therefore, only the T3 signature was consistently associated with poorer OS and DFS across both datasets. We next considered whether the T3 neutrophil signature was also associated with poorer OS in other solid tumors. Within the TCGA pan-cancer database (*57*), higher expression of the T3 signature was associated with a significantly higher risk of death across a subset of solid cancers, including pancreatic cancer [from the The Cancer Genomics Atlas Pancreatic Adenocarcinoma (TCGA-PAAD); see Fig. 6L and table S7 for *P* values and confidence intervals]. By contrast, T1 and T2 signatures were both protective against (lower hazard ratios, HRs) or associated with (higher HRs) patient death depending on the type of solid tumor (Fig. 6L and table S7), which is consistent with their nature as transitional subsets in the process of reprogramming. These data support a model in which tumor-educated T3 neutrophils drive tumor progression in both mouse and human cancers.

## Discussion

Environmental cues can fine-tune immune responses by inducing cell recruitment and expansion of immune cells, generating productive responses with adequate numbers and specialized phenotypes. Unable to further proliferate, neutrophils rely on their ability to swiftly mobilize into tissues to perform their functions effectively, and in diseases such as cancer, neutrophils at various maturation stages, tissue origins, and phenotypes are recruited into the tumor in large numbers (*12*–*14*, *17*, *19*). Given the likely coexistence of multiple tumor neutrophil states with different functional phenotypes, it is thus unclear how neutrophils exert a focused local effect in the tumor. Here, we examined how neutrophils decouple their initial maturation phenotype from their eventual protumoral function by undergoing convergent reprograming within the tumor.

Our study demonstrates that tumor-infiltrating immature and mature neutrophils acquire distinct epigenetic, transcriptomic, and proteomic phenotypes while retaining features of their initial maturation status. We found that both immature (T1) and mature (T2) tumor neutrophils within the tumor converged toward a third population (T3) expressing dcTRAIl-R1. T3 neutrophils thus show intermediate maturation scores when quantified at the population level, and have both toroidal (immature) and hypersegmented (mature) neutrophil nuclei, representative of their being an admixture of reprogrammed neutrophils of T1 and T2 origin. Our data reveal the capacity of neutrophils to simultaneously integrate different types of signals from the environment, allowing them to layer a new functional phenotype onto their pre-existing differentiation stage. We demonstrated this plasticity with immature and mature neutrophils from tumor-naïve mice, which are both capable of acquiring phenotypic (dcTRAIL-R1 expression) and transcriptional traits of the T3 state when cultured in tumor-conditioned medium or upon entering the tumor in vivo. By circumventing neutrophil maturation as a rate-limiting step, this adaptability allows immature neutrophils to be equally mobilized and reprogrammed within the tumor in a shorter time frame. Subsequently, this intrinsic ability embedded in neutrophils consolidates the various functional neutrophil states into one terminal neutrophil phenotype as directed by the tissue, in this case, a tumor.

Circulating neutrophils have a predicted half-life of ~10 hours (58), whereas tissue-resident neutrophils persist for up to 1 day (49). Although studies have hinted that neutrophils persist far longer within the tumor (10, 59, 60), whether this coincides with terminal differentiation in the tumor remains an open question. Using a BrdU pulse-labeling approach, we found that up to 5% of the originally labeled neutrophils could remain within the tumors for as long as 5.625 days upon entry. In addition, whereas our curve fit was accurate for the first labeling time points, there was a noticeable underfitting at 12 and 15 days after labeling, representing a possible underestimation of the full tumor neutrophil life span and indicating that a small population of neutrophils could persist even longer within the tumor. Long-lived neutrophils were predominantly of the dcTRAIL-R1$^{hi}$ T3 phenotype, which indicates a correlation between their ability to survive within challenging hypoxic and glycolytic environments and their continued persistence within the tumor. Spatial mapping at the transcriptome and protein level placed T3 neutrophils predominantly within a hypoxic-glycolytic niche nearer to the tumor core. By contrast, T1 and T2 neutrophils were positioned at the stromal and tumor parenchyma, where a large vessel network exists, supporting the notion that these cell states are in the process of reprogramming after tumor entry. Given that hypoxia is not required to trigger T3 reprogramming, which can occur in normoxic conditions, we propose that migration toward the hypoxic-glycolytic niche occurs after acquisition of T3 epigenetic and transcriptional programs is fully complete to ensure neutrophil survival. Consistent with this possibility, upstream transcription factors regulating metabolic and oxidative stress are switched on in T3 neutrophils compared with T1 or T2 populations. Deletion or inhibiting these transcription factors to trace the timeline of T3 reprogramming thus represent important goals for future studies within the field.

T3 neutrophils accelerated early tumor growth experimentally, and although we still observed tumor growth with other co-injected neutrophil subsets, this occurred at a slower rate, likely due to recruitment and reprogramming of endogenous T3 neutrophils at the later time points. T1 and T2 neutrophils did not show statistically significant enhancement or inhibition of tumor growth compared with other control neutrophil populations or phosphate-buffered saline (PBS), reflecting their transitional nature as opposed to a fully anti- or protumoral population. By contrast, the sustained growth advantage conferred by T3 neutrophils stemmed, at least in part, from T3-dependent remodeling of the vasculature toward the core of the tumor. Given their localization within the glycolytic-hypoxic niche, an intriguing scenario is that T3 neutrophils serve as possible guide rails to direct angiogenesis to relieve hypoxic and nutrient stress in areas that would most require it. Consistent with this, resistance toward anti-angiogenic therapies in human cancer has been associated with neutrophil infiltration (61), and neutrophil depletion reduces tumor vascularization and growth (51, 52, 62, 63). Studies facilitating further understanding of T3-mediated vascular remodeling would reveal new therapeutic targets against pathological angiogenesis within the tumor.

A particularly interesting finding is the conservation of this differentiation program in tumor-infiltrating neutrophils across tumor type and species. When scRNAseq datasets from other tumor models were examined, T3 annotation could identify protumoral clusters found both in mouse [i.e., mN5 (11)] and in human [i.e., TAN-1 (56)]. T3 neutrophils promoted PDAC tumor growth in mice, whereas ablation of T3 neutrophils or their pro-angiogenic function removed this growth advantage. In parallel, the T3 signature consistently predicted poorer patient outcomes in two independent human PDAC cohorts, as well as in a subset of other solid tumors. Thus, different studies converge upon our identification of a terminally differentiated neutrophil state, the signature of which might be used to better understand neutrophil function in cancer and possibly to predict tumor progression. We propose that the reported heterogeneity of neutrophils across tumors more likely reflects transitional states derived from populations at different stages of maturation and/or reprogramming.

Collectively, by ordering neutrophils through the lens of their ontogeny, we have assessed global neutrophil phenotypic heterogeneity through maturation stages, extramedullary sources, and the specialization of each neutrophil to each tissue (49). Although all of these states coexist within the tumor-bearing mouse, the neutrophil maturation trajectory remains unchanged, consistent with findings in other proinflammatory settings (19, 20, 64, 65). Therefore, whereas our findings do not fully exclude the possibility of neutrophil reprogramming outside of the tumor, they do suggest that it is unlikely that upstream changes in neutrophil progenitors specifically drive the formation of a protumoral neutrophil population. Instead, it is the intrinsic capacity of recruited neutrophils to adapt in response to the tumor environment regardless of their initial phenotype that allows them to adopt convergent trajectories to settle upon a final, protumoral state. This feed-forward loop thus ensures the continued supply and differentiation of long-lived, pro-angiogenic neutrophils that support tumor growth. Expanding from the results of our study, we propose that it is advantageous for tissues to induce functional homogeneity in neutrophils at the local scale to support tissue growth and function. This process is then hijacked by the tumor to favor a functional neutrophil state that promotes aberrant tumor growth. Our findings thus suggest a general mechanism by which short-lived effector cells such as neutrophils efficiently adjust their functions to meet the demands of a tissue, and that local neutrophil responses can be therapeutically targeted.

## Methods summary

### *scRNAseq*

Sorted total neutrophils (Lin$^-$CD45$^+$CD115$^-$Ly6C$^{low}$Siglec-F$^-$Gr1$^+$CD11b$^+$Ly6G$^+$) from the BM, spleen, blood, and tumor of mice bearing orthotopic pancreatic tumors [generated as described in (66)] were incubated with 0.5 μg of Totalseq-A anti-mouse Hashtag antibodies (BioLegend) per 100,000 cells for 30 min at 4°C. Cells were washed with fluorescence-activated cell sorting (FACS) buffer, spun down, and resuspended in PBS with 1% bovine serum albumin. Cells were pooled accordingly for 10X Genomics 3' (v3) sequencing on NovaSeq (Illumina) following the manufacturer's protocol. Sequencing reads were evaluated by FastQC and MultiQC. High-quality reads were aligned to the GRCm38 mm10-2020-A genome assembly and quantified using CellRanger (version 2.2.0, 10X Genomics). The gene expression matrix was analyzed in R using the Seurat package (4.0.5) (68). Hashtags were demultiplexed using CITE-seq-Count. Doublets and multiplets were filtered out, as well as unique molecular identifiers (UMIs) with two or more hashtags associated with them. UMIs with excess mitochondrial reads (>5%), number of features <200 (low read counts) and >4200 (outliers) were also removed. Normalization, scaling, and clustering were performed with the default Seurat pipeline. The destiny package (3.4.0.) was used for diffusion mapping (24). Velocity analysis was performed with scVelo (2.1.0) (26) using the default stochastic model and velocity vectors were projected onto the diffusion map embedding. Regulatory network analysis was carried out with PySCENIC (0.10.4) ([27]) in Python and exported for visualization in R.

### *High-parameter flow cytometry staining and analysis*

Pancreatic tumor single-cell suspensions pooled from five tumor-bearing mice were stained with a backbone panel of fluorophore-conjugated antibodies. The stained cell suspension was then distributed equally across all antibody wells in the LEGENDScreenTM kit (BioLegend). Staining and washing were performed according to the manufacturer's instructions. Cells were finally stained with 1 μM DAPI, and 1 million events per well were acquired. Flow cytometry standard (.fcs) files corresponding to each unique PE marker were compensated and analyzed using FlowJo software (BD Biosciences). Compensated live, $CD45^+$ singlets were analyzed using the InfinityFlow (1.4.0) in R ([28], [29]). The analysis was transferred back to FlowJo, where clusters were manually annotated and the imputed PE intensity values for each cluster were exported. The geometric mean was calculated for each cluster for heatmap plotting and comparison.

### *Spatial transcriptomics for orthotopic pancreatic tumors*

Frozen tumor samples were quartered, embedded in optimal cutting temperature filled molds, and sectioned to a thickness of 10 μm at −20 °C. To ensure capture of tumor-infiltrating neutrophils, cryosections were screened for Ly6G immunofluorescence before mounting on Visium Spatial Gene Expression Slides (10X Genomics). Tissue sections were fixed with methanol; stained for cytokeratin, Ly6G, and DAPI; and imaged (EVOS Auto FL2, Thermo Scientific). After imaging, Visium Spatial Gene Expression libraries were prepared according to the manufacturer's protocol. Libraries were sequenced using HiSeq X or NovaSeq 6000 S4 (Illumina) at PE150 with 50,000 read pairs per tissue-covered spot. Fastq data were processed with SpaceRanger (version 1.2.2, 10X Genomics) and mapped to the GRCm38 mm10-2020-A genome assembly. Spots were filtered to remove DAPI-low/negative necrotic areas with Loupe browser 6 (10X Genomics). Downstream analysis was performed with Seurat (v3.2.3) with default parameters, and joint clustering was performed with BayesSpace ([36]). The cell2location package ([38]) was used for deconvolution. The UCell package ([80]) was used to score spots independently for enrichment in various GO processes.

### *MICS sample preparation and data analysis*

Tumor cryosections were fixed in 4% paraformaldehyde for 10 min, washed in PBS, and permeabilized for 20 min in blocking buffer (5% donkey serum, 0.3% Triton X-100, and DAPI). Sections were iteratively stained with fluorescein isothiocyanate (FITC)-, PE- and allophycocyanin (APC)-conjugated anti-mouse antibodies, after which image acquisition and processing was performed on the MACSima instrument as described previously ([39]). Images were preprocessed with MACS iQView software. Stitched and registered TIFF files of individual channels were then imported into Imaris (Bitplane). Staining artifacts were masked using the surface/spot tool, and the masked channel was exported back to MACS iQView. Image segmentation based on DAPI-stained nuclei was performed using the Advanced Tissue Morphology method with the donut algorithm and confirmed by visual inspection. Identified cells and related features containing marker intensities for all channels were imported into FlowJo to gate relevant populations. Seurat V4 was used for further visualization and cell-type annotations, and SPIAT ([48]) was used for distance-based and colocalization metrics determining neutrophil subset localization with the tumor.

### *In vitro cell culture*

TCM was collected from the culture of FC1242L PDAC cell lines, spun down at 1000*g* for 10 min at 4°C to pellet down dead cells and debris, after which the supernatant was aliquoted and stored at −20°C. A total of $2.5 \times 10^5$ sorted neutrophils per well were cultured in cDMEM (Gibco) or TCM in normoxia or in a hypoxia incubator at 5% $O_2$. After 1 and 3 days, dcTRAIL-R1 upregulation was analyzed by flow cytometry or wells were pooled, counted, and lysed for analysis of RNA expression.

### *BrdU pulse-chase assay*

Mice were injected intraperitoneally with 2 mg of BrdU (Sigma-Aldrich) at the indicated time points. To detect BrdU incorporation, cells from the BM, spleen, blood, and tumor in pancreatic tumor-bearing mice were stained with fixable vitality dye (LIVE/DEAD Fixable Blue Dead Cell Stain Kit, Invitrogen) and surface makers. Cells were then fixed, permeabilized, and finally stained intracellularly with FITC-conjugated anti-BrdU antibody according to the manufacturer's protocol before analysis with flow cytometry.

### *Subcutaneous pancreatic tumor model*

A total of $1 \times 10^5$ tumor cells were resuspended with or without with $1 \times 10^5$ neutrophils (specified in text) in 1× PBS, mixed in a 1:3 ratio of Matrigel, and injected subcutaneously into the right flanks of mice using a 30-gauge insulin needle. At 3 and 7 days after the initial injection, $1 \times 10^5$ neutrophils were resuspended in 30 μL of PBS and injected directly into the observable Matrigel-tumor plug. If antibodies were co-injected alongside neutrophils, 10 μg of antibody was added to $1 \times 10^5$ neutrophils and incubated for 10 to 20 min on ice before the addition of $1 \times 10^5$ tumor cells. From day 14 after the injection of the tumor, tumors were measured weekly with Vernier calipers and tumor volumes were calculated using the following formula: $0.5 \times \text{length} \times \text{width}^2$. Mice were euthanized at day 28 after injection and tumor presence and weights were recorded. Tumors were marked as rejected if there was complete absence of tumor formation or only a clear Matrigel plug left.

To evaluate vessel network formation in co-injected tumors, tumors were excised, fixed with 4% paraformaldehyde overnight at 4°C, and then washed with PBS. Samples were permeabilized with the SHANEL method, blocked, and finally stained for CD31 and propidium iodide (PI). Samples were then subjected to solvent-based optical clearing and transferred into ethyl cinnamate for imaging. All tumors were fully imaged from one lateral edge to the other at 2.0× magnification. Images were acquired using a lightsheet LaVision Ultramicroscope II and captured using the PCO edge 4.2 sCMOS camera and then analyzed using Imaris 9.5.0 (Bitplane). Total tumor volume imaged was first determined by surfacing positive PI signal using the surface function. To standardize the tumor volume evaluated, all tumor images were processed to obtain the same percentage volume (~35%) from the tumor midpoint, which was then used for the downstream analysis. The same image thresholds were applied consistently across tumors within the same experiment. Surfaces based on $CD31^+$ vessel staining were then created with a standardized seed point value of 16.2, and their distribution from tumor edge to the tumor midpoint was calculated using the shortest distance function. Finally, to quantify the vessels present, the total tumor length was then divided into percentile bins (10%), after which $CD31^+$ surface intensity was quantified and normalized against the total tumor volume intensity for each bin.

## REFERENCES AND NOTES

1. L. G. Ng, R. Ostuni, A. Hidalgo, Heterogeneity of neutrophils. *Nat. Rev. Immunol.* **19**, 255–265 (2019). doi: 10.1038/s41577-019-0141-8; pmid: 30816340
2. A. J. Gentles *et al*., The prognostic landscape of genes and infiltrating immune cells across human cancers. *Nat. Med.* **21**, 938–945 (2015). doi: 10.1038/nm.3909; pmid: 26193342
3. V. Bronte *et al*., Recommendations for myeloid-derived suppressor cell nomenclature and characterization standards. *Nat. Commun.* **7**, 12150 (2016). doi: 10.1038/ncomms12150; pmid: 27381735
4. J. Y. Sagiv *et al*., Phenotypic diversity and plasticity in circulating neutrophil subpopulations in cancer. *Cell Rep.* **10**, 562–573 (2015). doi: 10.1016/j.celrep.2014.12.039; pmid: 25620698
5. B. E. Hsu *et al*., Immature low-density neutrophils exhibit metabolic flexibility that facilitates breast cancer liver metastasis. *Cell Rep.* **27**, 3902–3915.e6 (2019). doi: 10.1016/j.celrep.2019.05.091; pmid: 31242422
6. J.-I. Youn, S. Nagaraj, M. Collazo, D. I. Gabrilovich, Subsets of myeloid-derived suppressor cells in tumor-bearing mice. *J. Immunol.* **181**, 5791–5802 (2008). doi: 10.4049/jimmunol.181.8.5791; pmid: 18832739

7. T. Condamine *et al.*, Lectin-type oxidized LDL receptor-1 distinguishes population of human polymorphonuclear myeloid-derived suppressor cells in cancer patients. *Sci. Immunol.* **1**, aaf8943 (2016). doi: 10.1126/sciimmunol.aaf8943; pmid: 28417112
8. C. Engblom *et al.*, Osteoblasts remotely supply lung tumors with cancer-promoting SiglecF$^{high}$ neutrophils. *Science* **358**, eaal5081 (2017). doi: 10.1126/science.aal5081; pmid: 29191879
9. F. Veglia *et al.*, Fatty acid transport protein 2 reprograms neutrophils in cancer. *Nature* **569**, 73–78 (2019). doi: 10.1038/s41586-019-1118-2; pmid: 30996346
10. C. Pfirschke *et al.*, Tumor-promoting Ly-6G+ SiglecFhigh cells are mature and long-lived neutrophils. *Cell Rep.* **32**, 108164 (2020). doi: 10.1016/j.celrep.2020.108164; pmid: 32966785
11. R. Zilionis *et al.*, Single-cell transcriptomics of human and mouse lung cancers reveals conserved myeloid populations across individuals and species. *Immunity* **50**, 1317–1334.e10 (2019). doi: 10.1016/j.immuni.2019.03.009; pmid: 30979687
12. H. Alshetaiwi *et al.*, Defining the emergence of myeloid-derived suppressor cells in breast cancer using single-cell transcriptomics. *Sci. Immunol.* **5**, eaay6017 (2020). doi: 10.1126/sciimmunol.aay6017; pmid: 32086381
13. F. Veglia *et al.*, Analysis of classical neutrophils and polymorphonuclear myeloid-derived suppressor cells in cancer patients and tumor-bearing mice. *J. Exp. Med.* **218**, e20201803 (2021). doi: 10.1084/jem.20201803; pmid: 33566112
14. M. Evrard *et al.*, Developmental analysis of bone marrow neutrophils reveals populations specialized in expansion, trafficking, and effector functions. *Immunity* **48**, 364–379.e8 (2018). doi: 10.1016/j.immuni.2018.02.002; pmid: 29466759
15. Y. P. Zhu *et al.*, Identification of an early unipotent neutrophil progenitor with pro-tumoral activity in mouse and human bone marrow. *Cell Rep.* **24**, 2329–2341.e8 (2018). doi: 10.1016/j.celrep.2018.07.097; pmid: 30157427
16. I. Kwok *et al.*, Combinatorial single-cell analyses of granulocyte-monocyte progenitor heterogeneity reveals an early uni-potent neutrophil progenitor. *Immunity* **53**, 303–318.e5 (2020). doi: 10.1016/j.immuni.2020.06.005; pmid: 32579887
17. H. Q. Dinh *et al.*, Coexpression of CD71 and CD117 identifies an early unipotent neutrophil progenitor population in human bone marrow. *Immunity* **53**, 319–334.e6 (2020). doi: 10.1016/j.immuni.2020.07.017; pmid: 32814027
18. D. E. Muench *et al.*, Mouse models of neutropenia reveal progenitor-stage-specific defects. *Nature* **582**, 109–114 (2020). doi: 10.1038/s41586-020-2227-7; pmid: 32494068
19. X. Xie *et al.*, Single-cell transcriptome profiling reveals neutrophil heterogeneity in homeostasis and infection. *Nat. Immunol.* **21**, 1119–1133 (2020). doi: 10.1038/s41590-020-0736-z; pmid: 32719519
20. T. E. Khoyratty *et al.*, Distinct transcription factor networks control neutrophil-driven inflammation. *Nat. Immunol.* **22**, 1093–1106 (2021). doi: 10.1038/s41590-021-00968-4; pmid: 34282331
21. C. Wu *et al.*, Spleen mediates a distinct hematopoietic progenitor response supporting tumor-promoting myelopoiesis. *J. Clin. Invest.* **128**, 3425–3438 (2018). doi: 10.1172/JCI97973; pmid: 29771686
22. M. Liu *et al.*, PERK reprograms hematopoietic progenitor cells to direct tumor-promoting myelopoiesis in the spleen. *J. Exp. Med.* **219**, e20211498 (2022). doi: 10.1084/jem.20211498; pmid: 35266960
23. S. R. Hingorani *et al.*, Trp53R172H and KrasG12D cooperate to promote chromosomal instability and widely metastatic pancreatic ductal adenocarcinoma in mice. *Cancer Cell* **7**, 469–483 (2005). doi: 10.1016/j.ccr.2005.04.023; pmid: 15894267
24. P. Angerer *et al.*, destiny: Diffusion maps for large-scale single-cell data in R. *Bioinformatics* **32**, 1241–1243 (2016). doi: 10.1093/bioinformatics/btv715; pmid: 26668002
25. L. Haghverdi, M. Büttner, F. A. Wolf, F. Buettner, F. J. Theis, Diffusion pseudotime robustly reconstructs lineage branching. *Nat. Methods* **13**, 845–848 (2016). doi: 10.1038/nmeth.3971; pmid: 27571553
26. G. La Manno *et al.*, RNA velocity of single cells. *Nature* **560**, 494–498 (2018). doi: 10.1038/s41586-018-0414-6; pmid: 30089906
27. B. Van de Sande *et al.*, A scalable SCENIC workflow for single-cell gene regulatory network analysis. *Nat. Protoc.* **15**, 2247–2276 (2020). doi: 10.1038/s41596-020-0336-2; pmid: 32561888
28. C.-A. Dutertre *et al.*, Single-cell analysis of human mononuclear phagocytes reveals subset-defining markers and identifies circulating inflammatory dendritic cells. *Immunity* **51**, 573–589.e8 (2019). doi: 10.1016/j.immuni.2019.08.008; pmid: 31474513
29. E. Becht *et al.*, High-throughput single-cell quantification of hundreds of proteins using conventional flow cytometry and machine learning. *Sci. Adv.* **7**, eabg0505 (2021). doi: 10.1126/sciadv.abg0505; pmid: 34550730
30. K. Neumann *et al.*, Clec12a is an inhibitory receptor for uric acid crystals that regulates inflammation in response to cell death. *Immunity* **40**, 389–399 (2014). doi: 10.1016/j.immuni.2013.12.015; pmid: 24631154
31. W. Xu *et al.*, Immune-checkpoint protein VISTA regulates antitumor immunity by controlling myeloid cell–mediated inflammation and immunosuppression. *Cancer Immunol. Res.* **7**, 1497–1510 (2019). doi: 10.1158/2326-6066.CIR-18-0489; pmid: 31340983
32. S. V. Ryzhov *et al.*, Role of TGF-β signaling in generation of CD39+CD73+ myeloid cells in tumors. *J. Immunol.* **193**, 3155–3164 (2014). doi: 10.4049/jimmunol.1400578; pmid: 25127858
33. M. Casanova-Acebes *et al.*, Tissue-resident macrophages provide a pro-tumorigenic niche to early NSCLC cells. *Nature* **595**, 578–584 (2021). doi: 10.1038/s41586-021-03651-8; pmid: 34135508
34. S. Kaur *et al.*, Functions of thrombospondin-1 in the tumor microenvironment. *Int. J. Mol. Sci.* **22**, 4570 (2021). doi: 10.3390/ijms22094570; pmid: 33925464
35. A. I. Markowska, F.-T. Liu, N. Panjwani, Galectin-3 is an important mediator of VEGF- and bFGF-mediated angiogenic response. *J. Exp. Med.* **207**, 1981–1993 (2010). doi: 10.1084/jem.20090121; pmid: 20713592
36. E. Zhao *et al.*, Spatial transcriptomics at subspot resolution with BayesSpace. *Nat. Biotechnol.* **39**, 1375–1384 (2021). doi: 10.1038/s41587-021-00935-2; pmid: 34083791
37. W. Lu, Y. Kang, Epithelial-mesenchymal plasticity in cancer progression and metastasis. *Dev. Cell* **49**, 361–374 (2019). doi: 10.1016/j.devcel.2019.04.010; pmid: 31063755
38. V. Kleshchevnikov *et al.*, Cell2location maps fine-grained cell types in spatial transcriptomics. *Nat. Biotechnol.* **40**, 661–671 (2022). doi: 10.1038/s41587-021-01139-4; pmid: 35027729
39. A. Kinkhabwala *et al.*, MACSima imaging cyclic staining (MICS) technology reveals combinatorial target pairs for CAR T cell treatment of solid tumors. *Sci. Rep.* **12**, 1911 (2022). doi: 10.1038/s41598-022-05841-4; pmid: 35115587
40. Y. Kinugasa, T. Matsui, N. Takakura, CD44 expressed on cancer-associated fibroblasts is a functional molecule supporting the stemness and drug resistance of malignant cancer cells in the tumor microenvironment. *Stem Cells* **32**, 145–156 (2014). doi: 10.1002/stem.1556; pmid: 24395741
41. A. Costa *et al.*, Fibroblast heterogeneity and immunosuppressive environment in human breast cancer. *Cancer Cell* **33**, 463–479.e10 (2018). doi: 10.1016/j.ccell.2018.01.011; pmid: 29455927
42. R. J. Slack, R. Mills, A. C. Mackinnon, The therapeutic potential of galectin-3 inhibition in fibrotic disease. *Int. J. Biochem. Cell Biol.* **130**, 105881 (2021). doi: 10.1016/j.biocel.2020.105881; pmid: 33181315
43. E. Fonsatti, M. Altomonte, M. R. Nicotra, P. G. Natali, M. Maio, Endoglin (CD105): A powerful therapeutic target on tumor-associated angiogenetic blood vessels. *Oncogene* **22**, 6557–6563 (2003). doi: 10.1038/sj.onc.1206813; pmid: 14528280
44. A. Giatromanolaki *et al.*, Ectonucleotidase CD73 and CD39 expression in non-small cell lung cancer relates to hypoxia and immunosuppressive pathways. *Life Sci.* **259**, 118389 (2020). doi: 10.1016/j.lfs.2020.118389; pmid: 32898522
45. K. Losenkova *et al.*, Compartmentalization of adenosine metabolism in cancer cells and its modulation during acute hypoxia. *J. Cell Sci.* **133**, jcs241463 (2020). doi: 10.1242/jcs.241463; pmid: 32317394
46. N. Petruk *et al.*, CD73 facilitates EMT progression and promotes lung metastases in triple-negative breast cancer. *Sci. Rep.* **11**, 6035 (2021). doi: 10.1038/s41598-021-85379-z; pmid: 33727591
47. Z. Fu *et al.*, Proteolytic regulation of CD73 by TRIM21 orchestrates tumor immunogenicity. *Sci. Adv.* **9**, eadd6626 (2023). doi: 10.1126/sciadv.add6626; pmid: 36608132
48. Y. Feng *et al.*, Spatial analysis with SPIAT and spaSim to characterize and simulate tissue microenvironments. *Nat. Commun.* **14**, 2697 (2023). doi: 10.1038/s41467-023-37822-0; pmid: 37188662
49. I. Ballesteros *et al.*, Cooption of neutrophil fates by tissue environments. *Cell* **183**, 1282–1297.e18 (2020). doi: 10.1016/j.cell.2020.10.003; pmid: 33098771
50. L. Yang *et al.*, Expansion of myeloid immune suppressor Gr$^+$CD11b$^+$ cells in tumor-bearing host directly promotes tumor angiogenesis. *Cancer Cell* **6**, 13 (2004). pmid: 15488763
51. H. Nozawa, C. Chiu, D. Hanahan, Infiltrating neutrophils mediate the initial angiogenic switch in a mouse model of multistage carcinogenesis. *Proc. Natl. Acad. Sci. U.S.A.* **103**, 12493–12498 (2006). doi: 10.1073/pnas.0601807103; pmid: 16891410
52. F. Shojaei *et al.*, Bv8 regulates myeloid-cell-dependent tumour angiogenesis. *Nature* **450**, 825–831 (2007). doi: 10.1038/nature06348; pmid: 18064003
53. P. Kastana *et al.*, "Matrigel plug assay for in vivo evaluation of angiogenesis," in *The Extracellular Matrix*, D. Vigetti, A. D. Theocharis, Eds. (Springer, 2019), vol. 1952 of *Methods in Molecular Biology*, pp. 219–232; http://link.springer.com/10.1007/978-1-4939-9133-4_18.
54. V. Baeriswyl, G. Christofori, The angiogenic switch in carcinogenesis. *Semin. Cancer Biol.* **19**, 329–337 (2009). doi: 10.1016/j.semcancer.2009.05.003; pmid: 19482086
55. N. G. Steele *et al.*, Multimodal mapping of the tumor and peripheral blood immune landscape in human pancreatic cancer. *Nat. Cancer* **1**, 1097–1112 (2020). doi: 10.1038/s43018-020-00121-4; pmid: 34296197
56. L. Wang *et al.*, Single-cell RNA-seq analysis reveals BHLHE40-driven pro-tumour neutrophils with hyperactivated glycolysis in pancreatic tumour microenvironment. *Gut* **72**, 958–971 (2023). doi: 10.1136/gutjnl-2021-326070; pmid: 35688610
57. J. Liu *et al.*, An integrated TCGA pan-cancer clinical data resource to drive high-quality survival outcome analytics. *Cell* **173**, 400–416 (2018).
58. J. Pillay *et al.*, In vivo labeling with $2H_2O$ reveals a human neutrophil lifespan of 5.4 days. *Blood* **116**, 625–627 (2010). doi: 10.1182/blood-2010-01-259028; pmid: 20410504
59. Y. Sawanobori *et al.*, Chemokine-mediated rapid turnover of myeloid-derived suppressor cells in tumor-bearing mice. *Blood* **111**, 5457–5466 (2008). doi: 10.1182/blood-2008-01-136895; pmid: 18375791
60. P.-B. Ancey *et al.*, GLUT1 expression in tumor-associated neutrophils promotes lung cancer growth and resistance to radiotherapy. *Cancer Res.* **81**, 2345–2357 (2021). doi: 10.1158/0008-5472.CAN-20-2870; pmid: 33753374
61. L. M. Schiffmann *et al.*, Tumour-infiltrating neutrophils counteract anti-VEGF therapy in metastatic colorectal cancer. *Br. J. Cancer* **120**, 69–78 (2019). doi: 10.1038/s41416-018-0198-3; pmid: 30377339
62. J. Jablonska, S. Leschner, K. Westphal, S. Lienenklaus, S. Weiss, Neutrophils responsive to endogenous IFN-β regulate tumor angiogenesis and growth in a mouse tumor model. *J. Clin. Invest.* **120**, 1151–1164 (2010). doi: 10.1172/JCI37223; pmid: 20237412
63. Y. Itatani *et al.*, Suppressing neutrophil-dependent angiogenesis abrogates resistance to anti-VEGF antibody in a genetic model of colorectal cancer. *Proc. Natl. Acad. Sci. U.S.A.* **117**, 21598–21608 (2020). doi: 10.1073/pnas.2008112117; pmid: 32817421
64. R. Grieshaber-Bouyer *et al.*, The neutrotime transcriptional signature defines a single continuum of neutrophils across biological compartments. *Nat. Commun.* **12**, 2856 (2021). doi: 10.1038/s41467-021-22973-9; pmid: 34001893
65. E. Montaldo *et al.*, Cellular and transcriptional dynamics of human neutrophils at steady state and upon stress. *Nat. Immunol.* **23**, 1470–1483 (2022). doi: 10.1038/s41590-022-01311-1; pmid: 36138183

## ACKNOWLEDGMENTS

We acknowledge and thank all members of the L.G.N. laboratory for helpful discussion and feedback on the manuscript, the SIgN Flow Cytometry team for sorting and flow cytometry assistance, the SIgN Immunogenomics team for assistance with generating and running the ATACseq and scRNAseq libraries, and the SIgN mouse core facility for technical help and support. **Funding:** This research was funded by Singapore Immunology Network (SIgN) core funding and A*STAR, Singapore. L.G.N. is supported by National Natural Science Foundation of China (grant 32270956) and Shanghai Science and Technology Commission (grant 20JC1410100). M.S.F. is supported by the A*STAR Career Development Fund (grant 202D8150). I.W.K. is supported by the A*STAR Career Development Fund (grant 202D8197). S.Z.C. is supported by the A*STAR Career Development Award (192D8043) and core funding from SIgN. Y.T. and H.L.T. are supported by Clinician Scientist Awards (NMRC/CSA-INV/0023/2017 and CSAINV20nov-0003) from the National Medical Research Council of Singapore. The SIgN Flow Cytometry facility is supported by National Research Foundation (NRF) Singapore under Shared Infrastructure Support (SIS) (NRF2017_SISFP09). For the use of the Ultramicroscope II, we would like to thank A*STAR core funds, the HMBS IAF-PP grant (H1701a0004), and the National Research Foundation's Shared Infrastructure Support grant for SingaScope, a Singapore-wide microscopy infrastructure network (NRF2017_SISFP10), for continued support of the A*STAR Microscopy Platform. D.C.-W. is supported by a CRI Irvington postdoctoral fellowship (CRI3511). G.F.C. is supported by grant PID2022-142341OB-I00 funded by the Spanish MCIN/AEI/10.13039/501100011033. I.B. is supported by a Ramon y Cajal fellowship (RYC2021-033511-I) from MICINN and by a Leonardo fellowship (LEO22-2-2596) from the BBVA Foundation. A.V. and Y.Z. are supported by NMRC OF-IRG grant to VA (OFIRG19nov-0112). M.I. is supported by the European Research Council (ERC) Consolidator Grant 725038, ERC Proof of Concept Grants 957502 and 101138728, Italian Association for Cancer Research (AIRC) Grants 19891 and 22737, Italian Ministry for University and Research Grants PE00000007 (INF-ACT) and PRIN (2022FMESXL), and by a Funded Research Agreement from Asher Biotherapeutics and VIR Biotechnology. A.H. is supported by grant R01AI165661 from NIH/NIAD, RTI2018-095497- B-I00 from MCIN, HR17_00527 from Fundación La Caixa, the Transatlantic Network of Excellence (TNE-18CVD04) from the Leducq Foundation, and FET-OPEN (grant 861878) from the European Commission. The CNIC is supported by the MCIN and the Pro CNIC Foundation and is a Severo Ochoa Center of Excellence (CEX2020-001041-S). F.G. is supported by Singapore Immunology UIBR award from the Agency for Science, Technology and Research (A*STAR), a Singapore NRF Senior Investigatorship (NRFI2017-02), the Fondation Gustave Roussy, and the ARC Foundation. **Author contributions:** Conceptualization: L.G.N., M.S.F., L.T., I.W.K., A.H., F.G.; Formal analysis: K.B.D., V.N., J.M.C., M.W.L., L.X.J., B.Y.S., G.F.C.; Funding acquisition: L.G.N., M.S.F., I.W.K., Y.H.L.; Investigation: M.S.F., L.T., I.W.K., Y.R., C.M.S., K.L., Y.N.Z., J.J., K.H.L., D.H.L., Y.C.T., D.C.-W., K.Y., C.B., C.N.; Methodology: M.S.F., L.T., I.W.K., Y.R., C.M.S., D.C.-W., K.Y.; Project administration: L.G.N.; Supervision: L.G.N.; Visualization: M.S.F., L.T., I.W.K., Y.T., C.M.S., K.L., D.C.-W., K.Y.; Writing – original draft: L.G.N., M.S.F., L.T., I.W.K., A.H., F.G., D.C.-W.; Writing – review & editing: All authors **Competing interests:** M.S.F., L.T., F.G., and L.G.N. are inventors on patent WO2022132041 submitted by A*STAR that covers a method of characterizing an immunosuppressive neutrophils in cancer. M.I. participates in advisory boards and consults for Gilead Sciences, Third Rock Ventures, Antios Therapeutics, Asher Biotherapeutics, GentiBio, Clexio Biosciences, Sibylla Biotech, BlueJay Therapeutics, and Aligos Therapeutics. H.L.T. is a cofounder and medical adviser for RNAscence Pte. Ltd. F.G. participates in advisory boards for iTheos and Genoskin. The remaining authors declare no competing interests. **Data and materials availability:** All data needed to evaluate the conclusions in the paper are present in the paper and/or in the supplementary materials. scRNAseq (GSE243466), ATACseq (GSE244531), and spatial transcriptomics data (GSE244534) have been deposited in the NCBI Gene Expression Omnibus. All three datasets have been linked under into one SuperSeries GSE244536 for ease of access.

## SUPPLEMENTARY MATERIALS

science.org/doi/10.1126/science.adf6493
Materials and Methods
Figs. S1 to S16
Tables S1 to S7
References (*66*–*81*)
MDAR Reproducibility Checklist
Movies S1 and S2

Submitted 9 November 2022; resubmitted 23 August 2023
Accepted 27 November 2023
10.1126/science.adf6493